Molecular Cell

Article

BRD4-mediated ER membrane contact creates functionally distinct mitochondrial subtypes

Graphical abstract

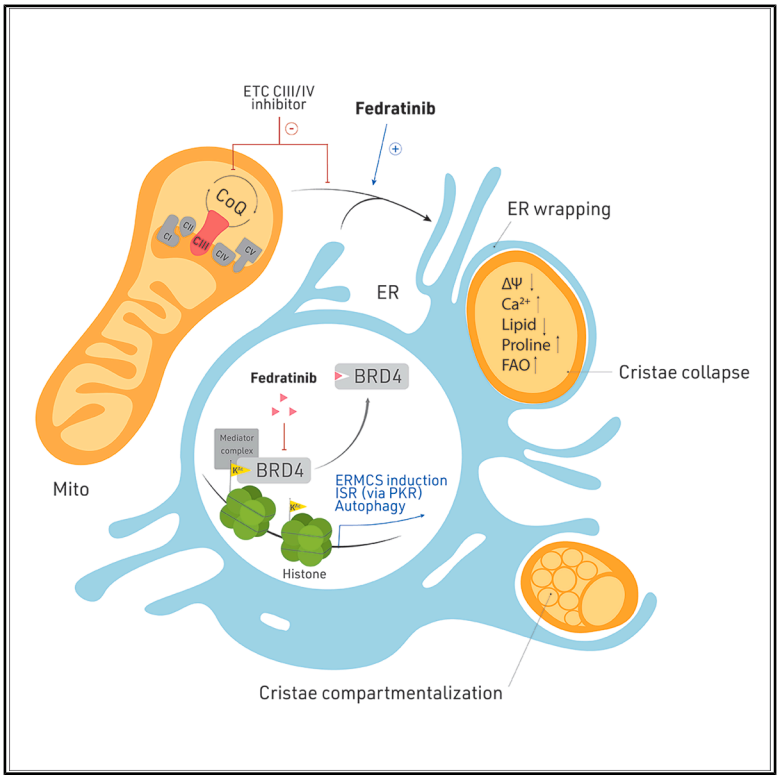

Highlights

- An image-based drug screen identified inducers of ER-mitochondria contacts (ERMCSs)
- BRD4 inhibition induces ERMCSs in a transcription-dependent manner
- BRD4-mediated ERMCSs form heterogeneous subpopulations of mitochondria
- BRD4-mediated ERMCSs require mitochondrial complex III activity and a balanced CoQ pool

Authors

Brandon Chen, Drew C. Stark, Pankaj V. Jadhav, ..., Tito Calì, Costas A. Lyssiotis, Yatrik M. Shah

Correspondence

clyssiot@umich.edu (C.A.L.), shahy@umich.edu (Y.M.S.)

In brief

Chen et al. used a reporter of endoplasmic reticulum-mitochondria contact sites (ERMCSs) to identify clinically relevant inducers of ERMCSs. They identified that fedratinib induces ERMCSs via inhibition of BRD4, requiring transcription and mitochondrial bioenergetics for ERMCS formation. Finally, the authors show BRD4-mediated ERMCSs create distinct intracellular mitochondria subpopulations.

Chen et al., 2026, Molecular Cell *86*, 917–936
March 5, 2026
https://doi.org/10.1016/j.molcel.2026.01.012

CellPress

Molecular Cell

CellPress
OPEN ACCESS

Article

BRD4-mediated ER membrane contact creates functionally distinct mitochondrial subtypes

Brandon Chen,[1,2] Drew C. Stark,[2,3] Pankaj V. Jadhav,[4,5] Theophilus M. Lynn-Nguyen,[6,7,8] Benjamin S. Halligan,[6,7] Nicholas J. Rossiter,[1,2] Nicole Sindoni,[9] Myungsun Shin,[9,10] Joao A. Paulo,[10] Matthew Chang,[4,5] Imhoi Koo,[11] Sergei Koshkin,[12] Sanjana Eyunni,[13,14,15] Paolo Ronchi,[16] Michelle T. Paulsen,[17] Harrison S. Greenbaum,[1,2] Mariana T. Ruckert,[2] Pietro Morlacchi,[18] David A. Hanna,[19] Jason Lin,[2] Rachel M. Guerra,[22]

(Author list continued on next page)

[1]Cellular and Molecular Biology Program, University of Michigan Medical School, Ann Arbor, MI 48109, USA
[2]Department of Molecular & Integrative Physiology, University of Michigan, Ann Arbor, MI 48109, USA
[3]Cancer Biology Program, University of Michigan Medical School, Ann Arbor, MI 48109, USA
[4]Life Sciences Institute, University of Michigan, Ann Arbor, MI 48109, USA
[5]Department of Cell and Developmental Biology, University of Michigan, Ann Arbor, MI 48109, United States
[6]Department of Medicinal Chemistry, College of Pharmacy, University of Michigan, Ann Arbor, MI 48109, USA
[7]Department of Internal Medicine, Division of Gastroenterology and Hepatology, Michigan Medicine at the University of Michigan, Ann Arbor, MI 48109, USA
[8]College of Pharmacy, University of Michigan, Ann Arbor, MI 48109, USA
[9]Division of Radiation and Genome Stability, Department of Radiation Oncology, Dana-Farber Cancer Institute, Harvard Medical School, Boston, MA, USA
[10]Department of Cell Biology, Harvard Medical School, Boston, MA, USA
[11]Department of Veterinary and Biomedical Sciences, Pennsylvania State University, University Park, State College, PA, USA
[12]Huck Institutes of the Life Sciences, Pennsylvania State University, University Park, State College, PA, USA
[13]Michigan Center for Translational Pathology, University of Michigan, Ann Arbor, MI 48109, USA
[14]Department of Pathology, University of Michigan, Ann Arbor, MI 48109, USA
[15]Molecular and Cellular Pathology Program, University of Michigan, Ann Arbor, MI 48109, USA
[16]Electron Microscopy Core Facility, European Molecular Biology Laboratory, 69117 Heidelberg, Germany
[17]Department of Radiation Oncology, University of Michigan, Ann Arbor, MI 48109, USA
[18]Agilent Technologies, Inc., Lexington, MA 02421, USA
[19]Department of Biological Chemistry, University of Michigan Medical School, Ann Arbor, MI 48109, USA

(Affiliations continued on next page)

SUMMARY

Inter-organellar communication is critical for cellular metabolism. One of the most abundant inter-organellar interactions occurs at the endoplasmic reticulum and mitochondria contact sites (ERMCSs). However, an understanding of the mechanisms governing ERMCS regulation and their roles in cellular metabolism is limited by a lack of tools that permit temporal induction and reversal. Through screening approaches, we identified fedratinib, an FDA-approved drug that dramatically increases ERMCS abundance by inhibiting the epigenetic modifier BRD4. Fedratinib rapidly and reversibly modulates mitochondrial and ER morphology, induces a distinct ER-mitochondria envelopment structure, and alters metabolic homeostasis. Moreover, ERMCS modulation depends on mitochondrial electron transport chain complex III function. Comparison of fedratinib activity to other reported inducers of ERMCSs revealed common mechanisms of induction and function, providing clarity to a growing body of experimental observations. In total, our results uncovered a novel epigenetic signaling pathway and an endogenous metabolic regulator that connects ERMCSs and cellular metabolism.

INTRODUCTION

The dynamic regulation of organelle networks and inter-organellar communication is critical for cellular metabolism and physiology. Direct inter-organellar communication occurs at membrane contact sites, which directly regulate metabolite transport, protein complex organization, signaling, and organellar function.[1,2] One of the most well-studied and abundant inter-organellar contact sites is endoplasmic reticulum-mitochondria contact sites (ERMCSs). While a wealth of research has defined

CellPress
OPEN ACCESS

Molecular Cell
Article

Tao Liu,[2] David J. Pagliarini,[20,21,22,23] Ruma Banerjee,[19] Abhijit Parolia,[3,13,14,24] Mats E. Ljungman,[3,17] Andrew D. Patterson,[11] Joseph D. Mancias,[9] Shyamal Mosalaganti,[4,5,19,26] Jonathan Z. Sexton,[6,7,8,27,28] Tito Calì,[29,30,31] Costas A. Lyssiotis,[1,2,3,7,25,*] and Yatrik M. Shah[1,2,3,7,25,32,*]

[20]Departament of Genetics, Washington University School of Medicine, St. Louis, MO 63110, USA
[21]Department of Biochemistry and Molecular Biophysics, Washington University School of Medicine, St. Louis, MO 63110, USA
[22]Department of Cell Biology and Physiology, Washington University School of Medicine, St. Louis, MO 63110, USA
[23]Howard Hughes Medical Institute, St. Louis, MO 63110, USA
[24]Department of Urology, University of Michigan, Ann Arbor, MI 48109, USA
[25]Rogel Cancer Center, University of Michigan, Ann Arbor, MI, USA
[26]Department of Biophysics, College of Literature, Science and the Arts, University of Michigan, Ann Arbor, MI 48109, USA
[27]Center for Drug Repurposing, University of Michigan, Ann Arbor, MI 48109, USA
[28]Michigan Institute for Clinical and Health Research, University of Michigan, Ann Arbor, MI 48109, USA
[29]Department of Biomedical Sciences, University of Padova, 35131 Padova, Italy
[30]Padova Neuroscience Center (PNC), University of Padova, 35131 Padova, Italy
[31]Center for Neurodegenerative Disease Research (CESNE), University of Padova, 35131 Padova, Italy
[32]Lead contact
*Correspondence: clyssiot@umich.edu (C.A.L.), shahy@umich.edu (Y.M.S.)
https://doi.org/10.1016/j.molcel.2026.01.012

the unique proteome at ERMCSs, the precise spatiotemporal regulation by various signaling pathways and evolutionarily conserved molecular tethering complexes that structurally support ER-to-mitochondria interactions still remains elusive. Functional genetic and biochemical studies have revealed essential roles of ERMCSs, including phospholipid synthesis,[3] calcium buffering,[4] mitochondrial dynamics,[5,6] mitochondrial DNA distribution,[7] and autophagosome formation.[8]

Dysregulation of ERMCSs and tethers contributes to the etiology of various diseases, including neurodegeneration,[9] obesity,[10] cancer,[11] diabetes,[12] and inborn errors of metabolism.[13] Understanding the fundamental mechanisms underlying ERMCS dysregulation is essential for identifying potential drug targets to restore ERMCS function in disease. However, significant gaps persist in our basic understanding of the molecular drivers governing the remodeling and organization of ERMCSs. Moreover, the exact mechanisms by which the microenvironment, signal transduction, and molecular cues initiate, maintain, and modify adaptive responses of ERMCSs are yet to be fully elucidated.

We identify a novel epigenetic and metabolic redox program regulating ERMCS formation and dynamics. We show that the FDA-approved drug fedratinib induces ERMCSs via bromodomain containing protein 4 (BRD4)-dependent histone recognition, providing a tool for reversible, temporal control of ERMCSs. Fedratinib promotes selective ER envelopment of mitochondria, accompanied by cristae defects, membrane potential loss, and metabolic rewiring. ERMCS induction requires mitochondrial complex III, a major site of coenzyme Q (CoQ) oxidation, and modulation of CoQ redox state suggests that increased reduced-to-oxidized CoQ may inhibit ERMCS formation. Finally, we demonstrate that the transcriptional and metabolic requirements for fedratinib-induced ERMCS are shared with other ERMCS-inducing stressors, revealing a conserved regulatory network.

RESULTS

High-throughput pharmacogenomic screening identifies novel regulators of ERMCSs

To visualize ERMCSs in living cells, we generated eleven isogenic cell lines expressing a doxycycline-inducible split-GFP-based ERMCS reporter (SPLICS) together with a mitochondrial matrix red fluorescent protein reporter (mitoTagRFP)[14–18] (Figure 1A). Selected clones exhibited inducible and reversible GFP fluorescence with stable RFP expression. Reporter induction did not affect cell growth, oxygen consumption, or extracellular acidification (Figures S1A–S1C). The SPLICS signal increased upon treatment with the ER stressor thapsigargin or expression of an artificial ER-mitochondria tether, confirming probe sensitivity and specificity[19] (Figures 1B and 1C). Control split-GFP probe pairs did not respond to thapsigargin (Figures S1D and S1E).[20]

Using SPLICS lines, we performed a high-content phenotypic imaging screen of an FDA-approved drug library (Figure 1D) (Table S1 and Zenodo: 10.5281/zenodo.13963526). In addition to known ER stressors,[21] we identified fedratinib as a potent ERMCS inducer. Fedratinib increased ERMCSs across multiple human and mouse cell lines (Figure 1E), with dose- and time-dependent effects validated by SPLICS (Figures 1F and 1G). Importantly, the increase in ERMCSs was reversible following a washout of fedratinib (Figure 1H). The extent of this reversibility was modestly dependent on cellular mitophagy programs (Figures S1G and S1H; see "limitations of the study" section). In addition, fedratinib did not significantly increase fluorescence of our control splitGFP probe pairs, nor did it induce autofluorescence when SPLICS is not activated (Figure S1F). We also tested for changes in GFP protein level associated with fedratinib and thapsigargin treatment after SPLICS activation. We observed increases in GFP expression approaching ~2-fold that, while evident, are modest relative to the 8–20-fold increase in SPLICS fluorescence observed upon treatment (Figure S1I). We validated the effect of fedratinib in inducing ERMCSs through inositol 1,4,5-triphosphoate receptor (IP3R)-translocase of outer mitochondrial membrane 20 (TOM20) interaction via proximity ligation assays (Figure S1J). Collectively, this screen identified the first FDA-approved drug with potent bioactivity in increasing ERMCSs across cell lines.

Bromodomain and extra-terminal protein-dependent transcription response is required for ERMCS induction

Fedratinib inhibits janus kinase 2 (JAK2) and (BRD4).[22–25] Other JAK2 inhibitors failed to induce ERMCSs, and genetic depletion

CellPress
OPEN ACCESS

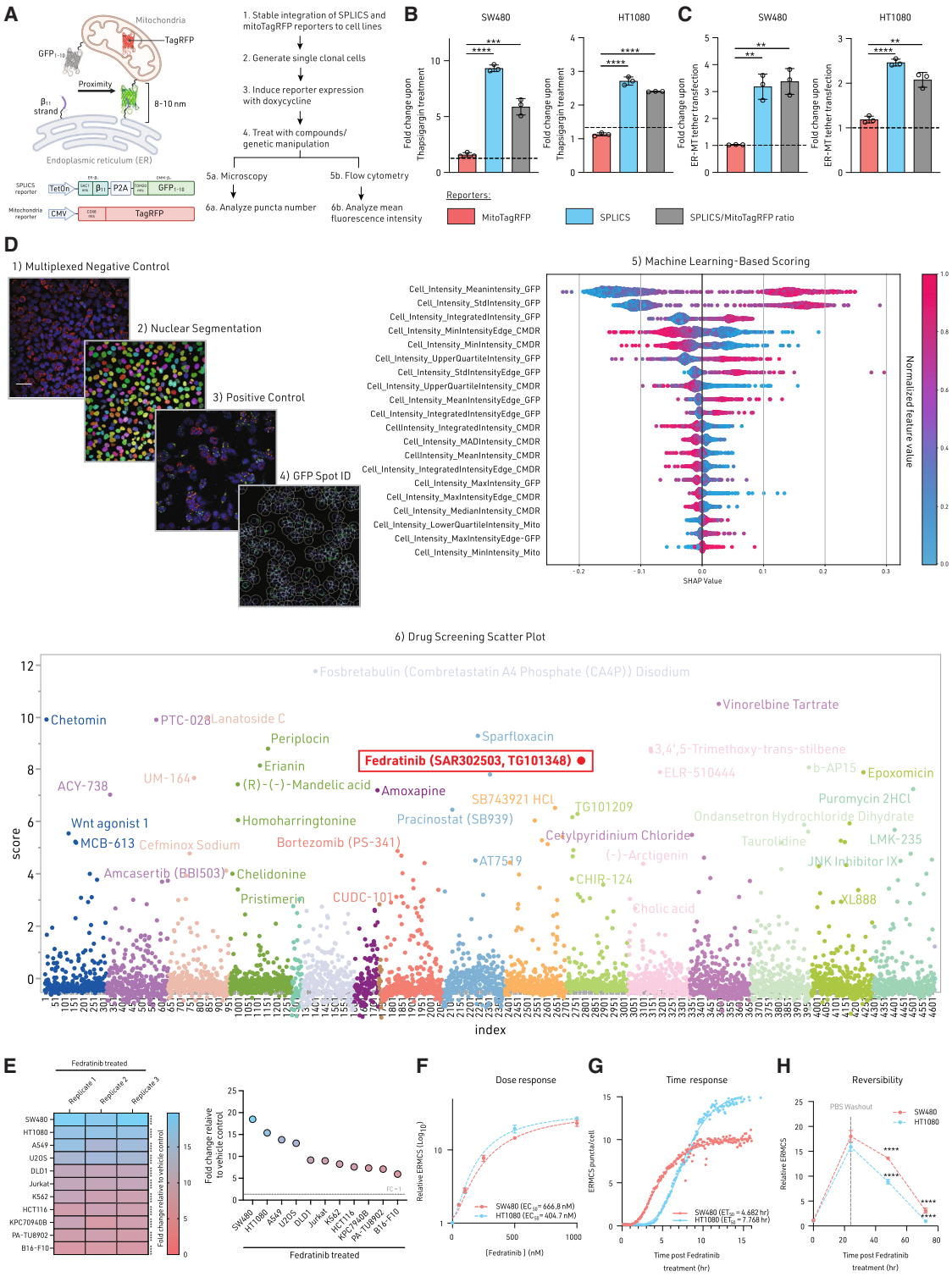

Figure 1. High-throughput image-based chemical screen identifies novel regulators of ERMCS

(A) Schematic of the SPLICS and mitochondria TagRFP (mitoTagRFP) reporter and analysis pipeline for ERMCS.

(B and C) (B) Relative fluorescence intensity of SPLICS, mitoTagRFP, and SPLICS/mitoTagRFP ratio following treatment with vehicle or thapsigargin (50 nM) for 24 h, or (C) 48 h post transfection of ER-MT tether.

(legend continued on next page)

of JAK2 did not block fedratinib responses (Figures 2A–2D). In contrast, BRD4 degradation or knockdown induced ERMCSs (Figures 2A–2C). Fedratinib rapidly suppressed MYC transcription and protein expression (Figures 2E, 2F, and S2A), consistent with BRD4 inhibition. Additional bromodomain and extra-terminal protein (BET) inhibitors also induced ERMCSs, whereas MYC inhibition alone did not (Figure S2B) (Zenodo: 10.5281/zenodo.13963526).

We conducted chromatin fractionation assays and found that fedratinib and the positive control BET inhibitor JQ1 displaced BRD4 from chromatin but not thapsigargin (Figure 2G). BRD4 chromatin immunoprecipitation (ChIP)-seq in SW480 cells identified that fedratinib has fewer BRD4-bound genomic loci in both promoter and non-promoter regions than thapsigargin (Figures 2H and 2I), and the BRD4-bound regions are mostly promoters, introns, or intergenic regions (Figure 2J). We then confirmed with ChIP-qPCR in HT1080 cells that fedratinib led to loss of BRD4 occupancy at the LncRNA plasmacytoma variant translocation (PVT) enhancer regions that control BRD4-hypersensitive gene MYC (Figure 2K).

Inhibition of cyclin-dependent kinases CDK8 and CDK9 (Figure 3A) or a pulse-chase experiment with RNA polymerase II (RNA pol II) inhibitor actinomycin D (ActD) suppressed ERMCS induction (Figures S2C and S2D), demonstrating that an active transcriptional program for ERMCS regulation is required. To identify BRD4 co-regulated complexes and transcription factors controlling ERMCSs, we performed an unbiased CRISPR screen using a nuclear genome library coupled with fluorescence-activated cell sorting (FACS). Cells transduced with genes annotated for nuclear localization or epigenetic regulation were treated with fedratinib, and those failing to induce ERMCSs (bottom 10% SPLICSlow/mitoTagRFP) were sorted (Figure 3B). Gene set enrichment analysis (GSEA) revealed strong signatures from mediator complex (MED) components (Figures 3C–3F; Table S2), a hetero-multimeric complex that recruits transcription factors, co-regulators, and RNA Pol II alongside BRD4. CRISPRi-mediated knockdown of MED16 or MED24 impaired ERMCS induction in response to fedratinib or thapsigargin (Figures 3G, 3H, and S3A).

bromouridine (BrU)-seq at 30-min and 2-h post fedratinib showed early upregulation of genes linked to the integrated stress response (ISR) and unfolded protein response (UPR), with ISR genes also increased at the protein level (Figures S3B–S3D; Table S3). However, fedratinib did not activate canonical UPR markers (phospho-PKR-like endoplasmic reticulum kinase [PERK], inositol-requiring enzyme 1 alpha [IRE1α], cell cycle progression 1 [CCPG1], activating transcription factor 6 [ATF6], spliced X-box binding protein 1 [XBP1], C/EBP homologous protein [CHOP], and binding immunoglobulin protein [BiP]) (Figure S3E), and chemical chaperone tauroursodeoxycholic acid (TUDCA) did not block ERMCS induction (Figure S3F), indicating fedratinib acts independently of UPR. Fedratinib increased ISR markers ATF4 and phosphorylated eukaryotic translation initiation factor 2 alpha (eIF2α) (Ser51) (Figure S3G). Screening eIF2α kinase activators revealed protein kinase RNA-activated (PKR) activation by 1H-benzimidazole1-ethanol,2,3-dihydro-2-imino-a-(phenoxymethyl)-3-(phenylethyl-,monohydrochloride (BEPP) as the most robust inducer of ERMCSs, while PKR inhibition reversed both ERMCS and ATF4 expression (Figures S3H and S3I). Integrated stress response inhibitor ISRIB reduced ATF4 but did not block ERMCSs (Figure S3J), suggesting fedratinib-induced ERMCSs rely on PKR but not ISR. Additionally, fedratinib did not activate UPR^{mito}, and activating mitochondrial ISR via oligomycin or carbonyl cyanide m-chlorophenyl hydrazone (CCCP) was not sufficient to induce ERMCS formation (Figures S3K and S3L).

Genes associated with autophagy were also upregulated by fedratinib. Consistent with BRD4 inhibition, fedratinib increased autophagy markers (microtubule-associated protein 1 light chain 3 beta (LC3B) lipidation) and lysosome abundance[8,26] with autophagic flux enhanced upon chloroquine (CQ) treatment (Figures S1H, S2E, and S2F). However, ERMCS formation persisted despite autophagy inhibition (CQ or bafilomycin A [BafA]), and SPLICS colocalization showed no overlap with autophagosomes or lysosomes (Figures S2G–S2I), indicating ERMCS induction is not an early mitophagy step.

Taken together, we have demonstrated that fedratinib induces ERMCSs via suppression of BRD4, and this activity is transcriptionally controlled. Moreover, induction of ERMCSs via the ER stressor thapsigargin also depends on an active gene expression program, indicating that transcriptional rewiring is common for other modes of ERMCS induction.

Fedratinib induces ER wrapping of mitochondria at ERMCSs

Organelle structures and inter-organellar organization networks inform the metabolic state of cells. An increase in ERMCSs drives adaptive oxidative phosphorylation and supports ER

(D) Schematic representation of the bioassay design for the ERMCS drug screen. Blue, Hoechst 33342/nuclei; red, mitoTagRFP/mitochondria; green, SPLICS/ERMCS. From upper left to bottom right: 1, negative control demonstrating low levels of ERMCS; 2, cellpose nuclear segmentation using Hoechst counterstain; 3, positive control demonstrating induction of high levels of ERMCS; 4, GFP spot identification and feature extraction using CellProfiler for ERMCS. Machine learning was performed by training an XGBoost model against per-plate controls; 5, Shapley additive explanations showing GFP features used to identify hits in drug screening. Beeswarm plot showing SHAP values indicating feature importance for drug effect scoring based on GFP features; 6, drug screening scatter plot showing drug tested on the *x* axis and XGBoost score on the *y* axis indicating ERMCS induction. Each color category for individual data points suggests different plates instead of categorization of drug pathways. Fedratinib is highlighted in red on the scatter plot. Scale bar, 15 μm.
(E) Relative ERMCS in a panel of cell lines treated with vehicle or fedratinib for 24 h.
(F) Dose-dependent increase of relative ERMCS of cells treated with vehicle or fedratinib for 24 h.
(G) Time-lapse imaging using lattice light sheet microscopy to monitor ERMCS puncta of cells treated with fedratinib for 16 h with quantified puncta per cell.
(H) Relative ERMCSs of cells treated with vehicle or fedratinib for 24 h, followed by PBS washout, and monitored for an additional 48 h maintained in doxycycline.
Experiments (B), (C), (E), (F), and (H) were performed three times, experiment (D) was performed once, and experiment (G) was performed twice. Significance was calculated with an unpaired two-tailed *t* test. $^{*}p \leq 0.05$, $^{**}p \leq 0.01$, $^{***}p \leq 0.005$, and $^{****}p \leq 0.001$. Data are mean ± SD. Statistical source data are provided in source data Figure 1.
See also Figure S1 and Table S1.

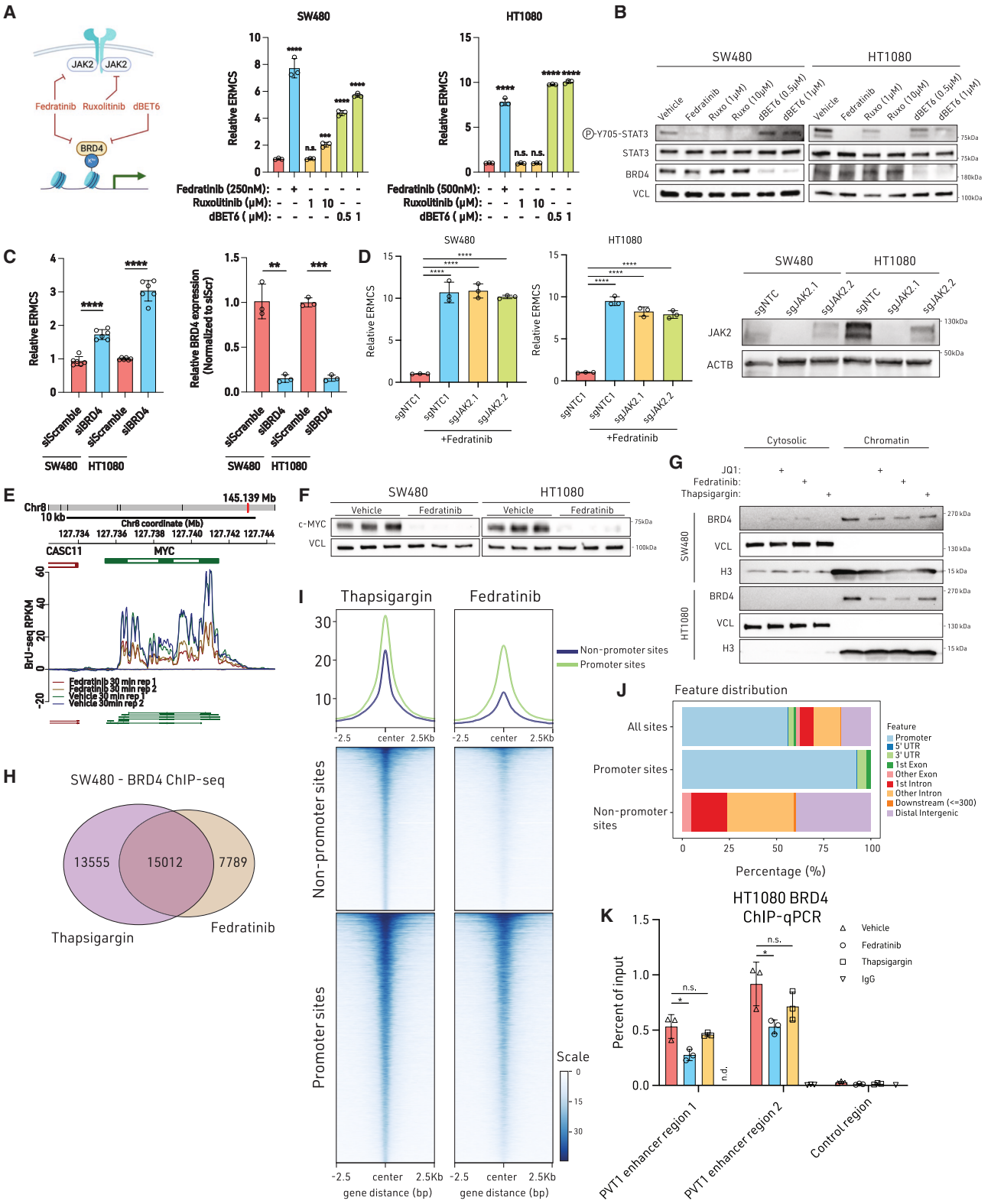

(legend on next page)

homeostasis. Therefore, we postulate that understanding how fedratinib impacts ERMCS architecture will provide valuable information for a deeper understanding of the metabolic factors, regulation, and consequences of ERMCS induction. To address this, we utilized various electron microscopy approaches to sequentially characterize ERMCS architecture.

From our transmission electron microscopy (TEM) on SW480 and HT1080 cells, we observed structural changes, such as the ER membrane enveloping mitochondria and cristae collapse and compartmentalization within the inner mitochondrial membrane (IMM) (Figure 4A). Approximately 15–20% of mitochondria exhibited complete cristae loss, and 40%–45% showed IMM compartmentalization (Figure 4A). Although we did not observe consistent changes in circular cross section, area, or aspect ratio, higher variability of these indices was seen in fedratinib-treated cells (Figures 4B–4D).

To further corroborate our observations and specifically probe ERMCSs, we performed correlative light and electron microscopy (CLEM) using the SPLICS reporter. We collected tilt series guided by ERMCS fluorescence in SW480 cells and reconstructed a 3D tomogram (Figures 4E and 4F). Fedratinib-treated cells, but not controls, exhibited direct juxtaposition of the ER and outer mitochondrial membrane (OMM) at SPLICS^{Hi} locations (Figure 4F), confirming TEM observations. We also observed near-complete collapse of the IMM/cristae at these contact sites. Typically, ERMCSs involve ER segments contacting the OMM rather than complete envelopment, but fedratinib induced striking ER-mitochondria engulfment, enhancing contact and promoting ultrastructural reorganization.

Our TEM and CLEM approaches revealed ER-enclosure structures around select mitochondria. To obtain higher-resolution volumetric information, we used high-pressure freezing followed by freeze-substitution and focused ion beam-scanning electron microscopy (FIB-SEM) on HT1080 cells. This preserves components in a near-native state, avoiding chemical fixation artifacts. FIB-SEM imaging was performed through half a cell volume at a 4-nm isotropic pixel size. We trained a deep-learning model to distinguish mitochondria and ER. Segmentation revealed mitochondria ensconced by ER in fedratinib-treated cells (Figure 4G). Consistent with light microscopy, we observed heterogeneous mitochondrial and cristae structures, including mitochondria lacking cristae or presenting swollen/circular inner membranes (Figure 4H). Overall, global mitochondrial volume, ERMCS distance, and ERMCS surface area were not significantly changed (Figures 4I–4K). Analysis of individual mitochondria showed a substantial increase in percent contact area (Figure 4L). Contact surface areas were comparable overall, but in fedratinib-treated samples, only a subset of mitochondria had smaller surfaces, indicating selective effects.

In conclusion, combining multiple electron microscopy modalities identified a novel ER-wrapped mitochondrial morphology in fedratinib-treated cells, characterized by a heterogeneous mitochondrial population with varying degrees of ERMCSs.

Metabolic and lipidomic changes associated with selective depolarization of ER-wrapped mitochondria

To visualize ERMCSs in a larger cellular context, intact mitochondria and ER networks, dynamics, and morphology in whole cells were imaged with light microscopy (LM). We found that a subset of mitochondria were rounded and swollen in fedratinib-treated cells and colocalized with ERMCS SPLICS reporter sites and ER marker Sec61 (Figures 5A and S4A), suggesting that very close proximity with the ER is needed to promote the above-mentioned ultrastructural reorganization of mitochondria. We termed mitochondria with high ERMCS SPLICS^{Hi} and those not associated with ERMCS as SPLICS^{Lo}. Expression of ER sheet and tubule-shaping proteins cytoskeleton-linking membrane protein 63 (CLIMP63/CKAP4) and reticulon-4 (RTN4) did not change (Figure S4B). SPLICS^{Lo} mitochondria with higher ERMCS distance still formed normal network-like morphology. OMM proteins (mitofusion 2 [MFN2], dynamin-related protein 1 [DRP1], and phospho-DRP1$^{S616/637}$), IMM organization proteins (optical atrophy 1 [OPA1], mitochondrial contact site, and cristae organizing system 60/25 [MIC60 MIC25]), and mitochondrial electron transport chain (ETC) expression did not change in whole-cell western blots (Figures S5A and S5B). These data suggest that structural changes induced by fedratinib are not likely the result of altered canonical mitochondrial dynamics or ER-shaping proteins, though membrane lipid remodeling cannot be excluded.

To further characterize mitochondrial function, we profiled mitochondrial mass, membrane potential (MMP/$\Delta\Psi$m), oxygen

Figure 2. ERMCS induction by fedratinib is dependent on BRD4, not JAK2

(A) Mechanisms of action for fedratinib, ruxolitinib, and dBET6 targeting JAK2 and BRD4 (left). Relative ERMCSs in cells treated with JAK2 and/or BRD4 inhibitors.
(B) Immunoblot from cells treated with vehicle, fedratinib (Fed), ruxolitinib (Ruxo), or dBET6 for 24 h.
(C) Relative ERMCS (left) and BRD4 mRNA expression of cells following knockdown (KD) using scrambled or BRD4-targeting siRNAs.
(D) Relative ERMCSs of control and JAK2 CRISPRi-KD cells (left) and immunoblot of JAK2 KD with CRISPRi in SW480 and HT1080 cells.
(E) Representative BrU-seq transcript profile on the MYC locus of SW480 cells treated with fedratinib or vehicle for 30 min.
(F) Immunoblot from cells treated with fedratinib for 24 h.
(G) Chromatin fractionation assay of cells treated with JQ1 (1 μM), fedratinib, and thapsigargin (50 nM) for 24 h.
(H) Venn diagram showing overlaps of BRD4 ChIP-seq in thapsigargin- (50 nM) vs. fedratinib-treated SW480 cells.
(I) ChIP-seq read density heatmaps of BRD4 at promoter and non-promoter sites in thapsigargin- (50 nM) vs. fedratinib-treated SW480 cells.
(J) Genomic locations of BRD4-bound sites defined from the overlap analysis in (H).
(K) BRD4 ChIP-qPCR analysis of BRD4-bound PVT1 enhancer regions in HT1080 cells treated with fedratinib or thapsigargin (50 nM) for 4 h.
Experiments (A)–(D) and (F) were performed three times, experiment (E) was performed once with duplicates, and experiments (G)–(K) were performed once with biological duplicates. Significance was calculated with an unpaired two-tailed *t* test and one-way ANOVA with Tukey correction for multiple comparisons. n.s. = not significant, $^{*}p \leq 0.05$, $^{**}p \leq 0.01$, $^{***}p \leq 0.005$, and $^{****}p \leq 0.001$. Statistical source data are provided in source data Figure 2. Immunoblot source data are provided in source blot Figure 2.
See also Figure S2.

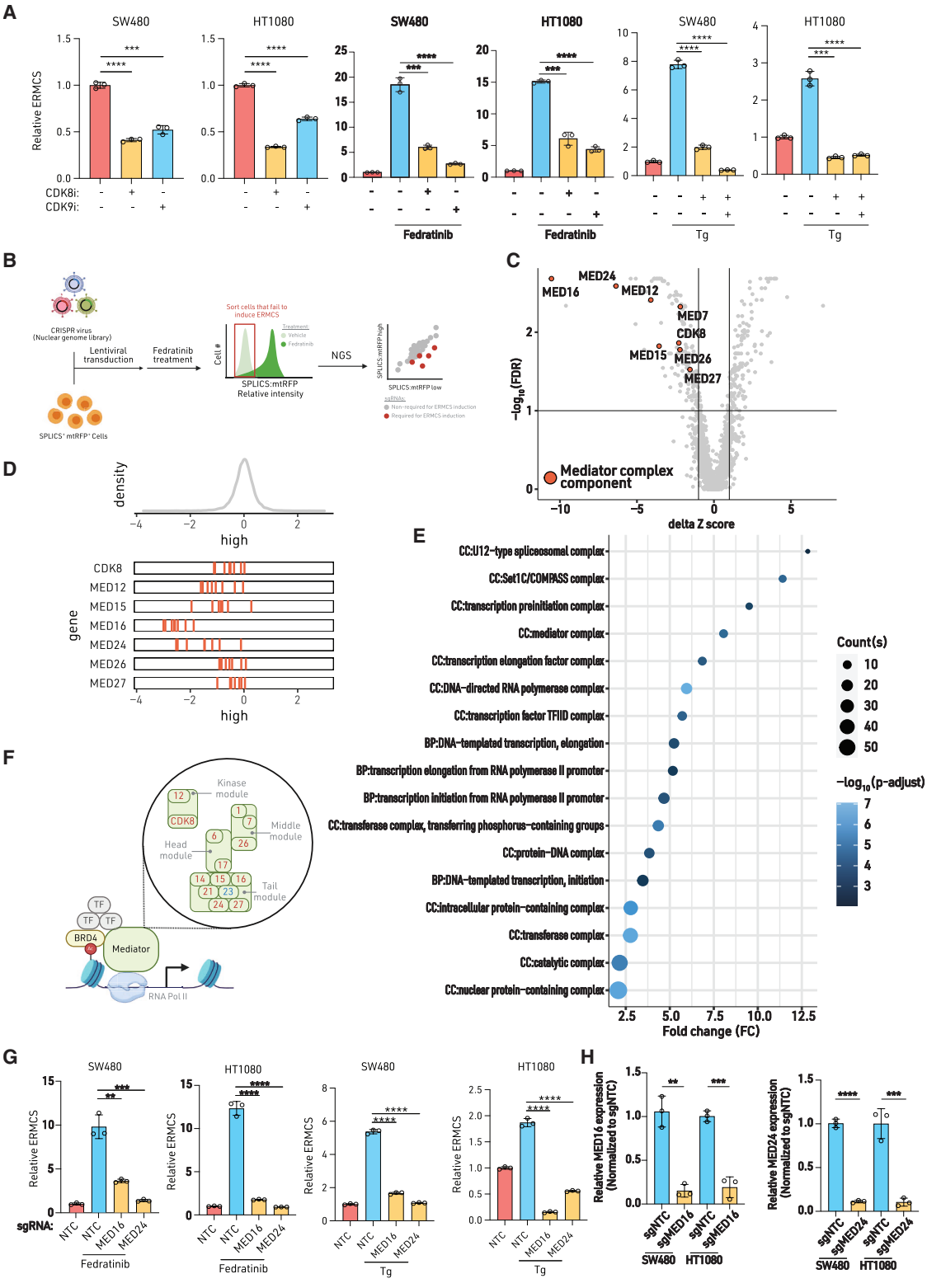

Figure 3. Inhibition of BRD4-mediated ERMCSs requires a transcriptional program dependent on the mediator complex

(A) Relative ERMCSs in cells treated with inhibitors of transcription kinase CDK8 (AS-2863619, 1 μM) or CDK9 (NVP2, 1 μM) for 6 h (left) and then treated with vehicle or fedratinib (middle) or thapsigargin (50 nM, right) for 24 h.

(legend continued on next page)

consumption rate (OCR), extracellular acidification rate (ECAR), mitochondrial reactive oxygen species (ROS), total cellular ROS, mitochondrial calcium response, and mtDNA content. We did not observe consistent differences between fedratinib- and control-treated cells in bulk whole-cell measurements (Figures S5C–S5G). Seahorse OCR analysis revealed variable changes in basal OCR, proton leak, and basal ECAR, but a consistent decrease in maximal respiration, ATP-linked respiration, and spare respiratory capacity (SRC) in both cell lines (Figures S5H–S5O), suggesting ERMCS induction by fedratinib could limit adaptive respiratory changes. Since these mitochondrial phenotyping approaches report changes in the average behavior at a whole-cell level, they could mask phenotypic differences since not all mitochondria are wrapped by ER in fedratinib-treated cells.

We next employed single-mitochondria functional profiling with fluorescence imaging, which revealed intracellular heterogeneity in mitochondrial membrane potential. Mitochondria wrapped with ER (SPLICS^{Hi}) have lower $\Delta\Psi$m compared with those lacking ERMCSs (SPLICS^{Lo}) (Figures 5A–5C and S4C). We did not observe changes in mitochondrial ROS at the single-mitochondrial or whole-cell level (Figures 5D–5F and S4C). Single-mitochondria flow cytometry further confirmed lower $\Delta\Psi$m when ERMCSs are induced that is absent at the whole-cell level (Figures 5H and 5I).

We next investigated the role of ERMCS induction by fedratinib on calcium homeostasis, since ER-to-mitochondria calcium transfer is one of the most well-established functions of ERMCSs. Using Rhod2 as a mitochondrial calcium indicator, we did not observe increased Rhod-2 signal upon fedratinib treatment, while inhibition of the mitochondrial calcium exporter sodium-calcium-lithium exchanger (NCLX) elevated Rhod-2 fluorescence (Figure S6A). With this data, we hypothesized that there could be heterogeneous mitochondrial populations with varying degrees of matrix calcium. We first validated that mitochondrial isolation followed by flow cytometry faithfully reports mitochondrial function by looking at reporter dyes for matrix calcium (Rhod-2) and mitochondrial membrane potential (Mitotracker Deep Red FM), along with control treatments such as CCCP for membrane potential and NCLX inhibition for Rhod-2 (Figure S6B). We then isolated Rhod2-stained mitochondria from fedratinib-treated cells and conducted flow cytometry analysis, as we did with membrane potential analysis. FACS analysis at the single-mitochondrial level revealed elevated mitochondrial calcium in SPLICS^{Hi} compared with SPLICS^{Lo} mitochondria (Figure S6C). Chelating intracellular calcium with BAPTA acetoxymethyl ester (BAPTA-AM) or inhibiting mitochondria calcium uniporter (MCU) did not affect ERMCS induction, suggesting mitochondrial calcium overload is a phenotype of ER-wrapped mitochondria (Figures S6D and S6E).

These points notwithstanding, we investigated the impact of fedratinib on whole-cell metabolism using metabolomics and lipidomics. Through dimensional reduction approaches to identify variability in metabolite and lipid profiles, we found that the metabolome is significantly altered upon induction of ERMCSs (Figure 5H; Table S4). Since loss of cardiolipin, a mitochondrial inner membrane lipid, or alteration in the phospholipid saturation state can directly affect cristae organization,[27] we also investigated changes in mitochondrial lipids upon fedratinib treatment. Changes to the lipidome were even more profound when we performed lipidomics on mitochondria isolated from fedratinib-treated cells, as we observed a dramatic decrease in mitochondrial lipids (Figure 5J; Table S5). From this analysis we identified a global decrease in lipids, particularly the structural phospholipid phosphatidylcholine (PtdCho) (Figure 5K).

Fedratinib induces subcellular proteomic changes specific to ER-enveloped mitochondria

To further explore mitochondrial heterogeneity within cells, we hypothesized that distinct mitochondrial populations with varying degrees of ER contact can be detected by fluorescence-activated mitochondrial sorting (FAMS). Although flow cytometric analysis of ERMCSs at the whole-cell level revealed continuous distribution, analysis at the individual mitochondrial level revealed two distinct populations with high and low levels of SPLICS intensity. Specifically, 36.98% of mitochondria in SW480 cells and 46.30% in HT1080 cells are SPLICS^{Hi}, whereas over 50% of mitochondria exhibited a low SPLICS signal (SPLICS^{Lo}) (Figure 6A). These data align with our microscopy data, which indicated only a subset of mitochondria were enveloped by the ER. Using FSC as a proxy of particle size, SPLICS^{Hi} mitochondria were larger than those not associated with the ER (Figures 6B and 6C).

To further identify mitochondrial proteomic heterogeneity, we conducted FAMS to isolate SPLICS^{Hi} and SPLICS^{Lo} mitochondria in fedratinib-treated cells relative to vehicle control (Figure 6D).[28] We enriched 90.8% of SPLICS^{Hi} in SW480 and 85.3% in HT1080 cells (Figures 6E and 6F). Quantitative

(B) Schematic of a fluorescence-activated cell sorting (FACS)-based CRISPR screen using a nuclear genome-targeted sgRNA library.
(C) Volcano plot of CRISPR screen sgRNAs. The *x* axis is the CRISPR gene scores (delta *Z* score) with *y* axis being $-\log_{10}$ of false discovery rate (FDR). Highlighted red circles are sgRNAs targeting the mediator complex components.
(D) Histogram indicating the distribution of sgRNA. Shown below is the relative enrichment of mediator complex genes.
(E) GSEA ridgeplot displaying significantly enriched (FDR < 0.01) protein complexes based on differential CRISPR screen scores. BP, biological processes. CC, cellular components.
(F) Schematic of the mediator complex and BRD4 in transcriptional regulation. Mediator components from the CRISPR library annotated in red demonstrate suppression of ERMCSs.
(G) Relative ERMCSs upon CRISPRi-mediated knockdown of MED16 and MED24 in cells treated with vehicle, fedratinib (left), or thapsigargin (50 nM, right) for 24 h.
(H) Relative gene expression level of MED16 (left) and MED24 (right) mRNA transcripts upon CRISPRi-mediated knockdown.
Experiments (A), (G), and (H) were performed three times, and experiments (B)–(E) were conducted once. Significance was calculated with an unpaired two-tailed *t* test. n.s. = not significant, $^{*}p \leq 0.05$, $^{**}p \leq 0.01$, $^{***}p \leq 0.005$, and $^{****}p \leq 0.001$. Data are mean ± SD. Statistical source data are provided in source data Figure 3. See also Figures S2 and S3 and Tables S2 and S3.

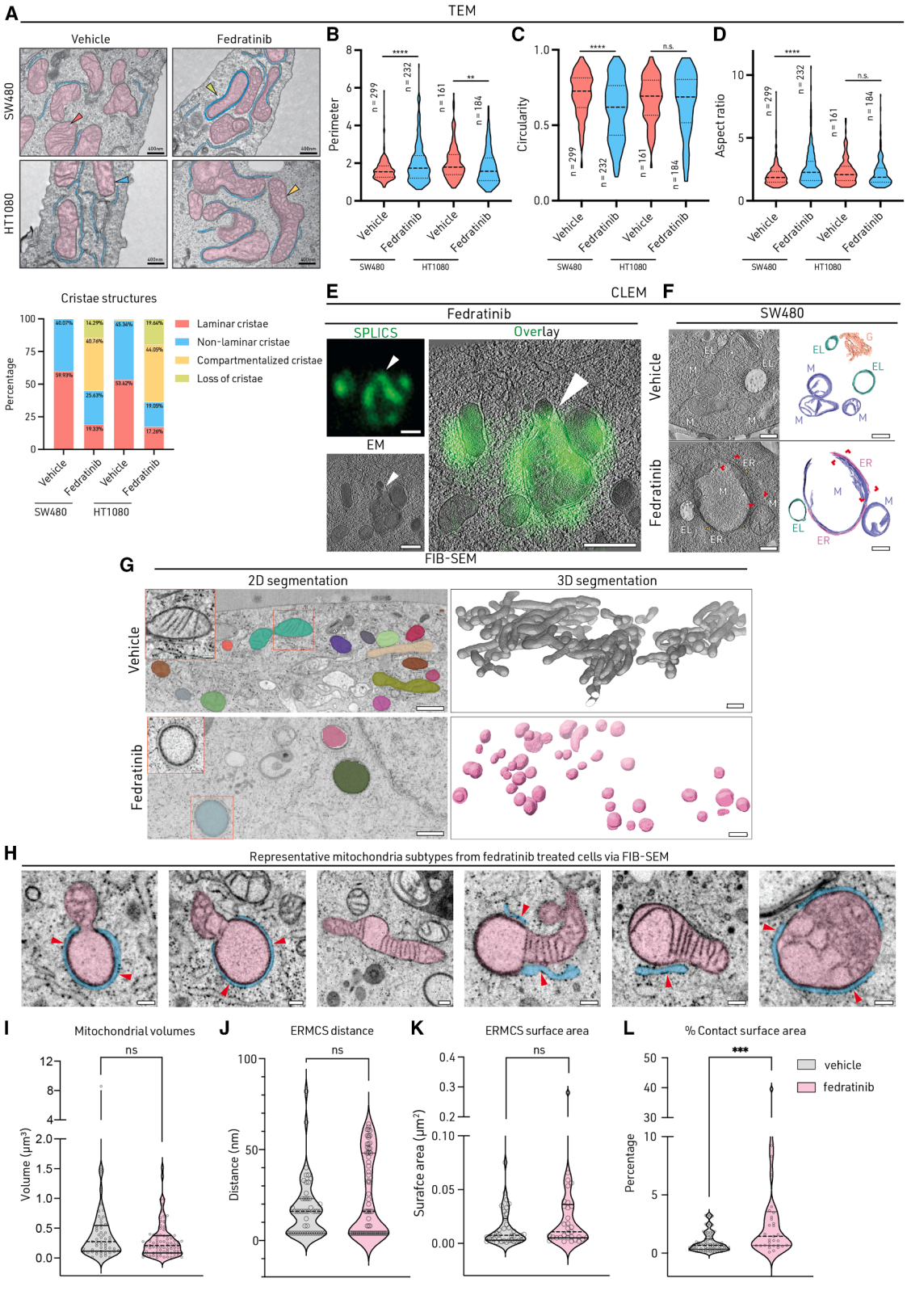

(legend on next page)

proteomics on FAMS-sorted mitochondria from SW480 cells enriched mitochondrial protein 3.8-fold relative to the whole-cell proteome (Figure 6G; Table S6). Fedratinib increased ER-localized proteins ~2-fold, and SPLICS^{Hi} mitochondria were enriched for ER proteins ~4.8-fold (Figures 6H–6J), supporting higher ER engagement. Gene ontology (GO) analysis identified enrichment of mitochondria, membranes, and organelles (Figure 6K).

In SPLICS^{Hi} mitochondria, we identified a strong enrichment of N-linked glycosylation machineries, including the catalytic subunits of the oligosaccharyltransferase (OST) complex dolichyl-diphosphooligosaccharide–protein glycosyltransferase subunits STT3A and B (STT3A/3B) and other OST components such as ribophorin 1 (RPN1) and magnesium transporter 1 (MAGT1) (Figure 6L). However, the identification of rough ER-associated N-glycosylation machinery (OST complex) and the ER-Golgi trafficking chaperone transmembrane p24 trafficking protein 9 (TMED9) suggests that the ER at these ERMCSs are not canonical ER tubules but rather rough ER sheets. Given that the cellular ER distribution follows a pattern of more sheets at the perinuclear region than the cell periphery, the distribution of our SPLICS-marked mitochondria is consistent with the current literature.

Additionally, mitochondrial proteins selectively enriched in SPLICS^{Hi} mitochondria included voltage-dependent anion channels (VDAC)1–3, which are known ERMCS tethers. We also identified enrichment of enzymes involved in reductive proline biosynthesis, aldehyde dehydrogenase 18A1 (ALDH18A1)/pyrroline-5-carboxylate synthase (P5CS), pyrroline-5-carboxylate reductase 1/2 (PYCR1/PYCR2), as well as fatty acid oxidation (FAO) proteins carnitine palmitoyltransferase 1A (CPT1A), acyl-CoA dehydrogenase very long chain (ACADVL), hydroxyacyl-CoA dehydrogenase A/B (HADHA/B), acetyl-CoA acetyltransferase 1 (ACAT1), and solute carrier 25A20 (SLC25A20). This suggests that mitochondria in contact with the ER could be involved in distinct metabolic processes compared with those that are not interacting with the ER (Figure 6L). Coiled-coil domain containing 51 (CCDC51), a mitochondrial inner membrane fission regulator, was upregulated in SPLICS^{Hi} mitochondria, potentially explaining the fragmented phenotype.[29] It is possible that outer membrane-associated fission protein DRP1 was lost during the FAMS process. Through our single-mitochondrial-level analyses, we have identified a unique proteome associated with mitochondria in physical contact with the ER.

ETC complex III function is necessary for ERMCS formation

Based on the drastic mitochondrial structural and less pronounced but significant metabolic changes associated with ERMCS induction, we hypothesized that an optimal metabolic state would be required to sustain metabolic demands for ERMCS formation. To test this model, we employed various mitochondrial perturbations and found that hypoxia reduced ERMCSs (Figure 7A). In addition to directly inhibiting oxygen-dependent reactions,[30] hypoxia also rewires cellular metabolism through hypoxia-inducible factors (HIFs). In contrast to hypoxia, HIF induction with the prolyl hydroxylase (PHD) inhibitor FG-4592 did not similarly attenuate fedratinib-induced ERMCSs, indicating that the hypoxia effect is independent of HIF activation but oxygen dependent (Figures 7A and S7A).

Since mitochondria are the largest oxygen consumers within the cell, we individually inhibited the ETC complexes I–V or depolarized membrane potential and then asked whether a specific ETC component is required for ERMCS induction (Figure 7B). Only complex III and IV inhibition suppressed the formation of ERMCSs induced by fedratinib (Figures 7C and 7D). We also report that complex III inhibition with antimycin A reversed mitochondrial PtdCho and lipid depletion from fedratinib treatment (Figures 7E and 7F), connecting regulatory patterns between ERMCSs and mitochondrial lipid regulation. As controls, we validated that antimycin A did not alter other SPLICS probes (Figure S7B).

Unlike ETC inhibitors that restrict oxygen consumption and generate mitochondrial ROS, inhibiting complexes III or IV suppresses the oxidation of CoQ/ubiquinol. Inhibition of complexes III and IV leads to the accumulation of $CoQH_2$, shifting the $CoQH_2$/CoQ pool toward a more reduced state. This reductive shift has been associated with reverse electron transport (RET)

Figure 4. Fedratinib induces ER wrapping of mitochondria at ERMCSs

(A) Representative TEM images (scale bar, 400 nm) of wild-type (WT) cells treated with vehicle or fedratinib for 24 h (organelle color mask on TEM, mitochondria in pink and ER in blue). Distribution of cristae morphologies quantified from 25 cells as a percentage of total mitochondria (n = 161–299) (below). Cristae structures are annotated in corresponding colors in the stacked bars, with the percentage of each classification listed. Red, laminar cristae. Blue, non-laminar cristae. Yellow, compartmentalized cristae. Green, loss of cristae. Each example cristae structure is indicated with its corresponding color in the EM images.

(B–D) Analysis of TEM images from (A) of (B) perimeter (μm), (C) circularity, and (D) aspect ratio of mitochondria in cells treated with vehicle or fedratinib for 24 h (n = 161–299).

(E) Correlative light and electron microscopy (CLEM) images of SW480 cells treated with fedratinib for 24 h (scale bar, 500 nm). White arrows indicate an example of SPLICS^{Hi} area.

(F) Segmentation of organelle membranes of SW480 cells treated with fedratinib for 24 h (M, mitochondria; ER, endoplasmic reticulum; EL, endolysosome; G, Golgi apparatus; red arrows, contact sites). Scale bar, 500 nm.

(G) Representative slices through the tomograms of vehicle control- (top left) and fedratinib-treated (bottom left) HT1080 cells with an overlay of 3D segmentation. Inset highlights a representative mitochondrion in each case. Scale bars, 200 nm and 50 nm for inset. 3D volume reconstructions (right) displaying mitochondria. Scale bar, 1 μm.

(H) FIB-SEM images showing instances of different morphologies of mitochondria wrapped around by ER membrane (red arrowheads). Scale bar, 200 nm. Organelle color mask on TEM, mitochondria in pink and ER in blue.

(I–L) (I) Quantification of total mitochondrial volume, (J) ER-mitochondria contact site intermembrane distances, (K) ER-mitochondria contact surface area, and (L) percentage contact surface area for individual mitochondria in vehicle-treated and fed-treated cells.

Experiments (A)–(L) were performed once. Significance was calculated with an unpaired two-tailed t test. n.s. = not significant and $^{***}p \leq 0.005$. Statistical source data are provided in source data Figure 4.

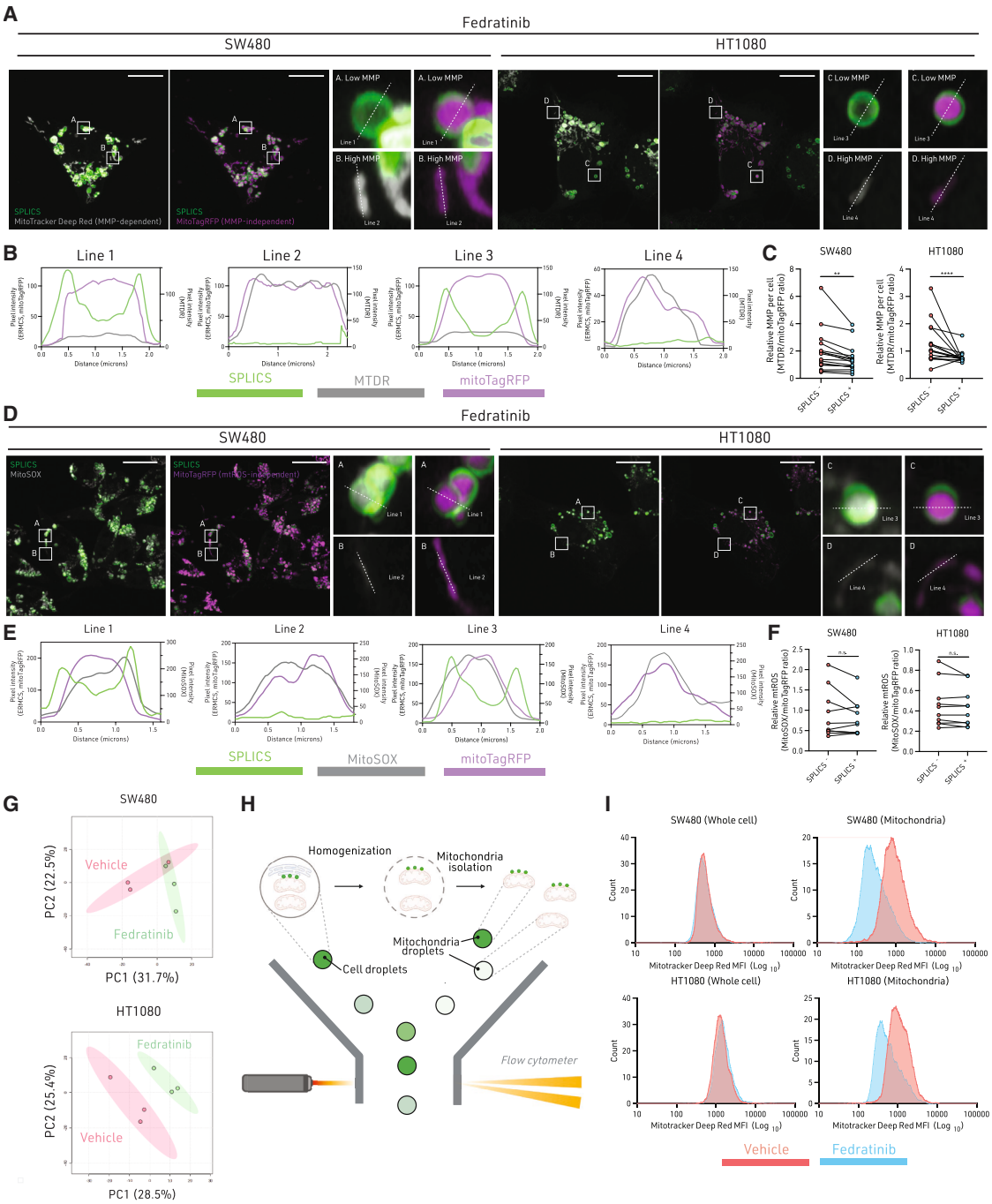

(legend on next page)

at complexes I and II, generating ROS and reducing fumarate to succinate.[31]

We found that the mitochondrial-specific ROS inducer mitoparaquat (mitoPQ) did not significantly suppress ERMCSs formation (Figure S7C). Moreover, blocking electron leak and superoxide generation at the complex III Q0 site with S3QEL-2 did not rescue antimycin-dependent ERMCS suppression (Figure S7D). Therefore, we hypothesized that complex III inhibition suppresses ERMCS formation due to accumulation of reduced $CoQH_2$ rather than ROS generation. To relieve $CoQH_2$ buildup, we genetically expressed a *Ciona intestinalis* alternative oxidase (AOX),[31] which oxidizes $CoQH_2$ to CoQ in an antimycin/myxothiazol-insensitive manner (Figure 7D). Notably, cells expressing AOX retained fedratinib-induced ERMCSs when subjected to complex III inhibitors (Figures 7G and S7E). This regulation is not limited to fedratinib, as thapsigargin- and BEPP-induced ERMCSs were similarly regulated (Figures S7F–S7H).

Surprisingly, fedratinib did not alter the $CoQH_2$/CoQ redox ratio or CoQ_{10} abundance at the whole-cell or mitochondrial level when measured by mass spectrometry and high-performance liquid chromatography (HPLC) (Figures S7I and S7J). This suggests that maintaining the ability for complex III to carry out CoQ oxidation, rather than total CoQ levels, is crucial for ERMCS induction. Through confocal microscopy, we also showed that ER-wrapped mitochondria are enriched with the CoQ biosynthetic enzyme COQ9, indicating a potential role in local CoQ channeling (Figure S7K).

In addition to AOX expression, we used an orthogonal approach to alter electron flow to complex III. Co-inhibiting complexes I and III limited CoQH2 generation, decreased the $CoQH_2$/CoQ ratio, and restored ERMCS inducibility (Figure 7H). However, inhibiting complex I failed to rescue ERMCS suppression caused by complex IV inhibitors, H_2S, or hypoxia (Figures S7L and S7M), likely due to sulfide:quinone oxidoreductase (SQOR)-mediated CoQ reduction and inhibited NADH-dependent electron flux.

These findings support that complex III-dependent CoQ oxidation influences dynamic ERMCS induction and represents a novel metabolic prerequisite for ERMCS formation.

DISCUSSION

Inter-organellar contact sites mediate local signaling events, whole-cell metabolism, and tissue physiology. The dysregulation of ERMCSs has been implicated in diseases including cancer, fragile X syndrome,[32] and Friedrich's ataxia.[13] Despite their critical role in maintaining metabolic homeostasis, the mechanisms governing the dynamics of ERMCSs remain elusive, at least in part due to the lack of potent inducers with temporal control. We identified fedratinib, an FDA-approved drug for myelodysplastic syndrome that robustly induced the formation of ERMCSs across diverse cell lines. We demonstrated that the relevant molecular target of fedratinib was the epigenetic regulator BRD4, and inhibition initiated an activating gene expression program that coordinated with the mediator complex to induce ERMCSs. Using iterative electron microscopy approaches, starting with TEM, CLEM, and then cryo-preserved FIB-SEM, we identified that ERMCSs exhibited novel ultrastructural changes in response to fedratinib. These changes included a tight and complete envelopment of the entire mitochondrial membrane at a subset of mitochondria. This is similar to ER-mitochondrial interactions observed following infection with human cytomegalovirus and SARS-CoV-2, metastatic melanoma cells, and fasted hepatocytes in the liver.[33–35]

Despite these structural alterations, no consistent changes were observed in various ER and mitochondrial functions at the whole-cell level. This is remarkable, given that approximately 30% of mitochondria exhibited massive structural alterations, indicating that "normal" mitochondria may compensate to support cell homeostasis when other mitochondria are dysfunctional. To dissect mitochondrial-level heterogeneity, we optimized a single-mitochondrial sorting pipeline to distinguish different mitochondrial populations. As we observed from our single-mitochondrial proteomics, mitochondria with abundant contact sites with the ER may potentially be dedicated to supporting specific metabolic pathways, including proline biosynthesis or beta oxidation. These results underscore the significance of considering mitochondrial heterogeneity in the study of ERMCSs. Moreover, through probing ETC function, we demonstrated that ERMCS formation is dependent on the

Figure 5. Metabolic and lipidomic changes associated with selective depolarization of ER-wrapped mitochondria

(A and B) (A) Confocal images and (B) line intensity profile of representative $SPLICS^{Hi}$ and $SPLICS^{Lo}$ mitochondria of mitochondrial membrane potential (MitoTracker Deep Red [MTDR]) and total mitochondrial mass (mitoTagRFP) in cells treated with fedratinib for 24 h. Scale bar, 15 μm.

(C) Ratiometric analyses of mitochondrial membrane potential from $SPLICS^{-}$ and $SPLICS^{+}$ mitochondria in the same cell. Cells treated with fedratinib for 24 h (n = 16). Each dot indicates one cell that was imaged.

(D) Representative confocal images of MitoSOX Deep Red-stained cells treated with vehicle and fedratinib for 24 h. Scale bar, 15 μm.

(E) Line intensity profile of representative $SPLICS^{Hi}$ and $SPLICS^{Lo}$ mitochondria.

(F) Ratiometric analyses of mitochondrial membrane potential via MitoSOX/mitoTagRFP ratio were performed on $SPLICS^{Hi}$ and $SPLICS^{Lo}$ mitochondria in cells following treatment with fedratinib for 24 h. (n = 10;). Each dot indicates one cell that was imaged.

(G) Principal-component analysis (PCA) of metabolomic analysis of cells treated with vehicle or fedratinib for 24 h.

(H and I) (H) Diagram describing the FACS analysis of mitochondria, and (I) flow cytometry performed on whole cell (n = 10,000) or isolated mitochondrial (n = 100,000) fraction from cells treated with vehicle or fedratinib for 24 h. Log_{10}-scaled MTDR mean fluorescence intensity (MFI) displayed on x axis and count on the y axis.

(J) Volcano plot of lipidome profiles in mitochondria isolated from SW480 and HT1080 cells treated with fedratinib for 24 h.

(K) Volcano plot of mitochondrial PtdCho species highlighted in green in cells treated with fedratinib for 24 h.

Experiments (A)–(C), (H), and (I) were repeated three times. Experiments (D)–(F) were performed twice. Experiment (G) was conducted in biological triplicates. Experiments (J) and (K) were conducted once with four biological replicates. Two-tailed paired t tests were performed on (C) and (F). n.s. = not significant, $^{**}p \leq 0.01$, and $^{****}p \leq 0.001$. Statistical source data are provided in source data Figure 5.

See also Figures S4 and S5 and Tables S4 and S5.

CellPress
OPEN ACCESS

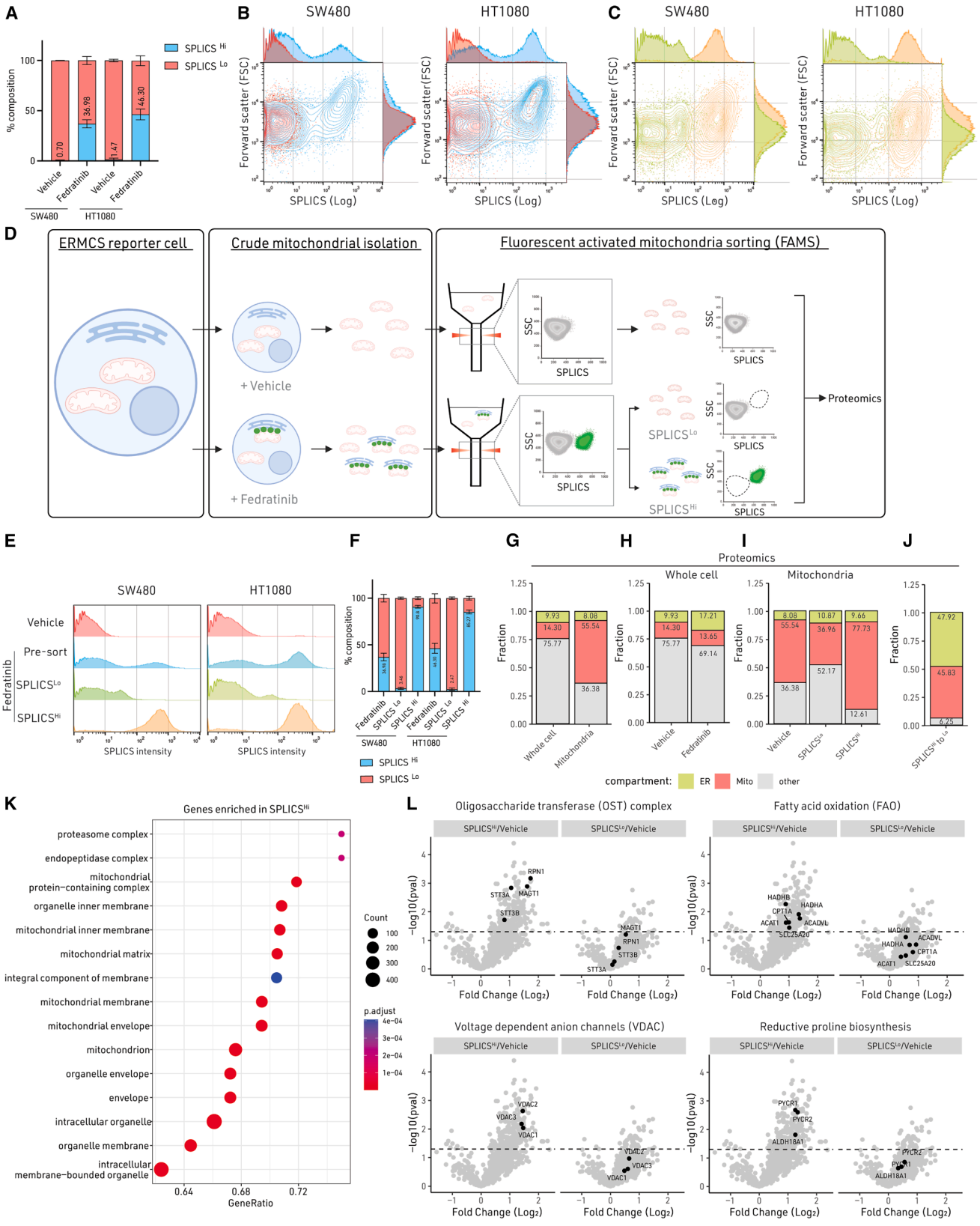

(legend on next page)

activity of mitochondrial complex III/IV. Methods bypassing their function restored ERMCS abundance, suggesting that non-affected mitochondria adapt or persist when complex III function is suppressed, whereas the affected mitochondria are targeted for ER engulfment.

Previous studies of BRD4 predominantly focused on its ability to act as a positive regulator of transcription.[36] In contrast, our findings demonstrate that de-repression of its target gene expression is required for ERMCS activity. Inhibition of BRD4 activates autophagy-related genes and corrects for mitochondrial disease phenotype by increasing mitochondrial biogenesis.[26,37] However, the direct transcriptional target(s) of BRD4 that regulate ERMCSs are not clear. Through transcriptomics we identified activation of the ISR in both cells with high basal ERMCSs and following fedratinib treatment. ISR activation relies on inducing PERK, heme-regulated inhibitor (HRI), general control nonderepressible 2 (GCN2), and PKR.[38] Recent work has demonstrated that mitochondrial stress and sublethal activation of mitochondrial outer membrane permeabilization (MOMP) can release cytochrome *c* and subsequently activate ISR.[39] Interestingly, the loss of cristae at ERMCSs resembles the effect induced by MOMP activation.[40] Moreover, the dynamic nature of ERMCSs is involved in apoptosis regulation and sensitivity.[41,42] Since the UPR can activate the ISR, we did an extensive comparison of fedratinib to thapsigargin. We did not observe UPR activation after fedratinib treatment nor changes in UPR targets (IRE1α, PERK, endoplasmic reticulum oxidoreductase 1 [ERO1L], and thioredoxin-related transmembrane protein 1 [TMX1]) that have been associated with ERMCS induction.[43–45] However, direct activation of the ISR kinase PKR induced ERMCSs, while inhibiting PKR suppressed fedratinib-induced ERMCSs. Interestingly, ISR inhibitor ISRIB decreased fedratinib-dependent ATF4 upregulation but failed to suppress ERMCSs. These findings reveal compelling connections between ISR signaling and ERMCS regulation, underscoring the complex interactions among eIF2α kinases and distinct cellular effects from early versus latent ISR activation.

Treatment with fedratinib induced the formation of ERMCSs and led to a significant decrease in mitochondrial lipids, particularly PtdCho. Mitochondrial PtdCho levels are dependent on lipid transfer from the ER to mitochondria, a process mediated by lipid transfer proteins such as vacuolar protein sorting-associated protein 13A (VPS13A) and StAR related lipid transfer domain containing 7 (STARD7). However, the dependency of mitochondrial lipid homeostasis on ER-mitochondria communication extends beyond PtdCho. For example, phosphatidylserine is transferred to mitochondria via extended synaptotagmins (E-Syt2/3) and oxysterol-binding protein related protein 5/8 (ORP5/8) at ERMCSs. Once inside mitochondria, phosphatidylserine can be decarboxylated to phosphatidylethanolamine, which is then transported back to the ER by currently uncharacterized lipid transfer proteins.

Intriguingly, inhibition of mitochondrial ETC complex III with antimycin A prevented the fedratinib-induced depletion of mitochondrial lipids. It is important to note that our lipidomic analysis was conducted on a crude mitochondrial fraction. Ideally, future studies will utilize FACS-sorted SPLICS^{Hi} and SPLICS^{Lo} mitochondria to differentiate the lipidome of ER-wrapped mitochondria from that of the general mitochondrial population. Nevertheless, the pronounced phenotype observed in the crude mitochondrial preparations strongly suggests a significant ETC complex III-dependent modulation of the mitochondrial lipidome specifically at ERMCSs.

The ratio of oxidized CoQ to reduced $CoQH_2$ plays a critical signaling role that reflects cellular metabolic states. While recognized as an electron carrier in the ETC,[46] CoQ has emerged as a multifunctional lipid involved in ferroptosis, pyrimidine biosynthesis, H_2S detoxification, glycerol phosphate shuttle, and proline catabolism.[47,48] Accumulation of $CoQH_2$ under hypoxia or sulfide exposure is essential to maintain tissue homeostasis by utilizing fumarate as a terminal electron acceptor instead of oxygen.[31,49] We demonstrated that ETC complexes III and IV could sustain a critical function needed for establishing ERMCSs. Utilizing genetic methods to bypass complex III inhibition via ectopic expression of AOX restored ERMCS abundance. Limiting electron entry from complex I reversed the inhibitory response of antimycin or myxothiazol and reactivated ERMCS induction. Based on the AOX and complex I/III

Figure 6. Fedratinib induces subcellular proteomic changes specific to ER-enveloped mitochondria

(A) Distribution of SPLICS^{Hi} and SPLICS^{Lo} mitochondria in fedratinib- and vehicle-treated cells.

(B) Scatter plot of individual mitochondria from fedratinib- and vehicle-treated cells with *x* axis as SPLICS MFI and *y* axis as forward scatter (FSC).

(C) Scatter plot of sorted mitochondria from fedratinib- and vehicle-treated cells with *x* axis as SPLICS MFI and *y* axis as FSC.

(D) Schematic of mitochondrial flow cytometry and sorting for proteomics.

(E) Histograms of pre- and post-sorted mitochondria from fedratinib- and vehicle-treated cells.

(F) Distribution of SPLICS^{Hi} and SPLICS^{Lo} mitochondria in pre- and post-sorted, fedratinib-treated cells.

(G) Subcellular proteomic distribution of ER, mitochondria, and other compartmental proteins in vehicle-treated whole cells and sorted mitochondria.

(H) Subcellular proteomic distribution of ER, mitochondria, and other compartmental proteins in fedratinib-treated whole cells.

(I) Subcellular proteomic distribution of ER, mitochondria, and other compartmental proteins in sorted vehicle-treated mitochondria, SPLICS^{Hi} mitochondria, and SPLICS^{Lo} mitochondria from fedratinib-treated cells.

(J) Subcellular proteomic distribution of ER, mitochondria, and other compartmental proteins comparing SPLICS^{Hi} to SPLICS^{Lo} mitochondria from fedratinib-treated cells.

(K) GSEA analysis of SPLICS^{Hi} mitochondria.

(L) Volcano plot showing enrichment of proteins involved in oligosaccharide transferase (OST) complex, fatty acid oxidation (FAO), voltage-dependent anion channel (VDAC), and reductive proline biosynthesis.

Experiments (A)–(C), (E), and (F) were performed three times, and experiments (G)–(L) were performed once with four biological replicates. Statistical source data are provided in source data Figure 6. Representative fluorescence-activated mitochondria sorting (FAMS) plots are provided in source FAMS Figure 6.
See also Figure S6 and Table S6.

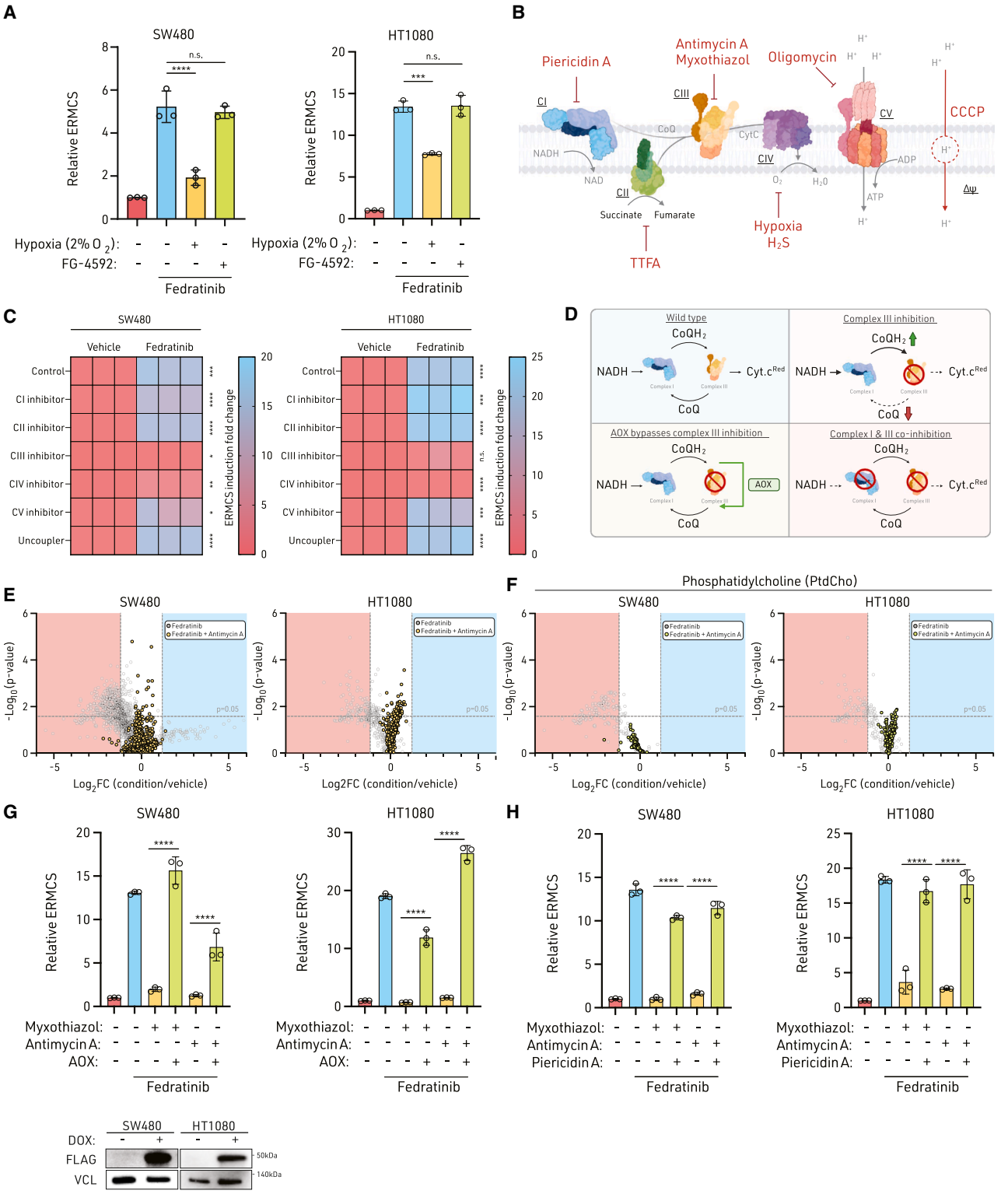

Figure 7. ETC complex III function is necessary for ERMCS formation

(A) Relative ERMCSs in cells incubated in hypoxia (2% O_2) or treated with a PHD inhibitor, FG-4592 (50 μM), for 48 h and then treated with fedratinib for 24 h. (B) Diagram of mitochondria electron transport chain (ETC) and specific mitochondrial complex inhibitors (CI, piericidin A [20 nM]; CII, TTFA [100 μM]; CIII, antimycin A [100 nM]; myxothiazol [50 nM]; CIV, hypoxia [2% O_2];H_2S [250 ppm]; CV, oligomycin; and uncoupler, CCCP).

(legend continued on next page)

co-inhibition results, we speculate a CoQ redox-sensing mechanism, as both rescue approaches should prevent $CoQH_2$ accumulation under complex III inhibition alone. Further studies to profile CoQ oxidation state on the subcellular level and spatial distribution will be critical for drawing definitive conclusions with the inconsistent change in CoQ redox state and CoQ abundance. Interestingly, it has been reported that loss of MFN2, a mitochondrial fusion factor and ERMCS tether, impairs CoQ production and complex III function.[50] Thus, we provide evidence to support that modulation of oxygen tension reorganizes the subcellular organellar landscape, and complex III function could potentially be an endogenous metabolic sensor for ERMCS formation. Importantly, while we made this discovery with fedratinib, we also illustrated that other ERMCS inducers, like the ER stressor thapsigargin, require the same molecular and metabolic mechanisms for ERMCS. This evidence suggests the mechanisms described here are broadly applicable to other ERMCS regulatory modalities.

Limitations of the study

While this study provides valuable insights into ER-mitochondria communication, limitations remain. Lipidomic analyses relied on crude mitochondrial fractions, and future studies using FACS-sorted $SPLICS^{Hi}$ and $SPLICS^{Lo}$ mitochondria will better define lipidomic changes specific to ER-wrapped mitochondria. These analyses will also define mechanisms by which fedratinib promotes ER-mitochondria tethering, especially considering the lack of canonical ERMCS tethers identified in our $SPLICS^{Hi}$ versus $SPLICS^{Lo}$ proteomics dataset. Secondly, as fedratinib indirectly inhibits BRD4 and activates ISR, some observed effects may not be exclusively attributable to ERMCS formation. Furthermore, ER-enveloped mitochondria in fedratinib-treated cells are structurally distinct from those formed by classical ERMCSs.[51] Future research employing more specific genetic or pharmacological tools to manipulate ERMCS formation would be valuable in dissecting the specific role of canonical ERMCS formation versus ER-mitochondria envelopment in the observed phenotypes.

Additionally, while the SPLICS reporter faithfully reports ER-mitochondria proximity induction, it was designed to report around an 8–10-nm distance. Additionally, SPLICS reversibility is on the scale of days (Figure 1H), implying a possibility of autophagic turnover (Figures S1G and S1H). As newer contact site reporters with improved reversibility and sensitivity under baseline conditions become available,[52,53] future studies employing these reporters are necessary to refine the molecular drivers of ERMCS regulation.

Despite these limitations, this study establishes a link between BRD4-dependent ERMCS regulation and mitochondrial lipid remodeling during cellular stress. In conclusion, we identify a tool compound that enables temporal modulation of ERMCSs and uncovers metabolic requirements underlying ER-mitochondria communication, laying a foundation for therapeutic targeting of inter-organellar signaling.

RESOURCE AVAILABILITY

Lead contact

Requests for further information and resources should be directed to and will be fulfilled by Yatrik Shah (shahy@umich.edu).

Materials availability

All unique/stable reagents generated in this study are available from the lead contact on request.

Data and code availability

- Image-based drug repurposing screen data has been deposited on Zenodo and are publicly available in the repository as part of this record: 10.5281/zenodo.13963526. Datasets generated are also available from the corresponding author upon reasonable request. BrU-seq data has been deposited to NCBI GEO under the accession number GSE: 278077. ChIP-seq data has been deposited to NCBI GEO under the accession number GSE: 280900. The mass spectrometry proteomics data have been deposited to the ProteomeXchange Consortium via the PRIDE partner repository with the dataset identifier PXD: 056917. Due to the size of the FIB-SEM data, it will be available upon request. All source data and additional supplemental data are uploaded to Mendeley Data at 10.17632/jc6wr2bry3.1.
- All original code is deposited at Zenodo and is publicly available as of the date of publication at 10.5281/zenodo.13963526.
- Any additional information required to reanalyze the data reported in this paper is available from the lead contact upon request.

ACKNOWLEDGMENTS

We thank all members of the Shah and Lyssiotis labs for their advice and suggestions. In collaboration with this research, we acknowledge support from the University of Michigan Biomedical Research Core Facilities (Flow Cytometry core, Advanced Genomics core, and Microscopy core) and Bru-seq lab. FIB-SEM imaging was performed in collaboration with the Advanced Imaging Center (AIC) at Janelia Research Campus, which is supported by the Howard Hughes Medical Institute, and particularly Dr. Jesse Aaron, Dr. Teng Leong Chew, Dr. Satya Khuon, and Leanna

(C) Relative ERMCSs (right) in cells treated with specific ETC inhibitors for 24 h and then treated with vehicle or fedratinib for 24 h.
(D) Diagram illustrating the regulation of CoQ redox state following complex III inhibition, expression of alternative oxidase (AOX) under complex III inhibition, and complex I/III dual inhibition.
(E) Volcano plot of isolated mitochondrial lipidome profiles comparing fedratinib (gray circle) and fedratinib plus antimycin A combination treatment (yellow dot).
(F) Volcano plot of mitochondrial PtdCho species in fedratinib (gray circle) and fedratinib plus antimycin A combination treatment (yellow dot).
(G) Relative ERMCSs in AOX-expressing cells treated with complex III inhibitors myxothiazol (50 nM) or antimycin A (100 nM) for 24 h and then treated with vehicle or fedratinib for 24 h. AOX expression was validated with immunoblotting (below).
(H) Relative ERMCSs in cells treated with complexes I and III inhibitors piericidin A (20 nM) and myxothiazol (50 nM) or antimycin A (100 nM) for 24 h and then treated with vehicle or fedratinib for 24 h.
Experiments (A, C, G, and H) were performed three times. Experiments (E and F) were performed once with four biological replicates. Significance was calculated with an unpaired two-tailed *t* test. n.s. = not significant, $^{**}p \leq 0.01$, $^{***}p \leq 0.001$, and $^{****}p \leq 0.001$. Data are mean ± SD. Statistical source data are provided in source data Figure 7. Immunoblot source data are provided in source blot Figure 7.
See also Figure S7.

Eisenmen for their help. The funders (Agilent Technologies) for the whole-cell metabolomics and lipidomics had no role in study design, data collection and analysis, or the content and publication of this manuscript. We acknowledge the European Molecular Biology Laboratory (EMBL) Electron Microscopy Core Facilities' assistance, data acquisition, and analysis for CLEM expertise. B.C. was supported by NCI F99CA284256-01. D.C.S. was supported by NIGMS 5T32GM145304-05. Y.M.S. was supported by NCI R01CA148828 and R01CA245546 and NIDDK R01DK095201. C.A.L. was supported by NCI R37CA237421, R01CA248160, and R01CA244931. S.M. was supported by NIGMS DP2GM150019. D.J.P. was supported by NIDDK R01DK098672 and NIGMS R35GM131795. N.J.R. was supported by NIGMS T32GM145470 and T32GM150581. H.S.G. was supported by NIGMS T32GM156550. R.B. was supported by NIGMS R35GM130183. D.A.H. was supported by NIGMS F32GM140694. A.D.P. was supported by NIH S10OD021750, USDA National Institute of Food, Federal Appropriations Project PEN04917, Accession 7006712, and Pennsylvania Department of Health using Tobacco CURE funds. T.C. was supported by the Italian Ministry of University and Research PRIN2017, University of Padova STARS Consolidator Grant 2019, Progetto di Ateneo 2023 no. CALI_BIRD23_01, and PNRR—CN3 National Center for Gene Therapy and Drugs based on RNA Technology no. CN00000041 (2022–26).

AUTHOR CONTRIBUTIONS

B.C., D.C.S., C.A.L., and Y.M.S. designed the study and wrote the manuscript. B.C. designed experiments and collected data for the bulk of the experimental studies. B.C., D.C.S., P.J., T.M.L.-N., B.S.H., N.J.R., N.S., M.S., J.A.P., M.C., M.T.P., H.S.G., M.T.R., S.K., I.K., S.E., P.R., P.M., D.A.H., J.L., R.M.G., and T.L. carried out experimental aspects of the project and contributed to data analysis. B.C., D.C.S., S.M., D.J.P., N.J.R., R.B., D.A.H., M.E.L., A.P., J.D.M., J.Z.S., T.C., C.A.L., and Y.M.S. provided resources, funding, and conceptual input for experiments and supervised the research. All authors were involved throughout the research process, agreed among themselves regarding roles and responsibilities, and contributed to the review, editing, and approval of the manuscript.

DECLARATION OF INTERESTS

In the past three years, C.A.L. has consulted for Astellas Pharmaceuticals, Odyssey Therapeutics, Third Rock Ventures, and T-Knife Therapeutics and is an inventor on patents pertaining to Kras-regulated metabolic pathways, redox control pathways in pancreatic cancer, and targeting the GOT1-ME1 pathway as a therapeutic approach (US Patent no. 2015126580-A1, 05/07/2015; US Patent no. 20190136238, 05/09/2019; International Patent no. WO2013177426-A2, 04/23/2015). J.D.M. reports research support from Novartis and Casma Therapeutics and has consulted for Third Rock Ventures and Skyhawk Therapeutics, all unrelated to the submitted work.

STAR★METHODS

Detailed methods are provided in the online version of this paper and include the following:

SUPPLEMENTAL INFORMATION

Supplemental information can be found online at https://doi.org/10.1016/j.molcel.2026.01.012.

Received: January 31, 2025
Revised: October 23, 2025
Accepted: January 7, 2026
Published: February 13, 2026

REFERENCES

1. Eisenberg-Bord, M., Shai, N., Schuldiner, M., and Bohnert, M. (2016). A Tether Is a Tether Is a Tether: Tethering at Membrane Contact Sites. Dev. Cell *39*, 395–409. https://doi.org/10.1016/j.devcel.2016.10.022.
2. Scorrano, L., De Matteis, M.A.D., Emr, S., Giordano, F., Hajnóczky, G., Kornmann, B., Lackner, L.L., Levine, T.P., Pellegrini, L., Reinisch, K., et al. (2019). Coming together to define membrane contact sites. Nat. Commun. *10*, 1287. https://doi.org/10.1038/s41467-019-09253-3.
3. Shiao, Y.J., Balcerzak, B., and Vance, J.E. (1998). A mitochondrial membrane protein is required for translocation of phosphatidylserine from mitochondria-associated membranes to mitochondria. Biochem. J. *331*, 217–223. https://doi.org/10.1042/bj3310217.
4. Hajnóczky, G., Robb-Gaspers, L.D., Seitz, M.B., and Thomas, A.P. (1995). Decoding of cytosolic calcium oscillations in the mitochondria. Cell *82*, 415–424. https://doi.org/10.1016/0092-8674(95)90430-1.
5. Friedman, J.R., Lackner, L.L., West, M., DiBenedetto, J.R., Nunnari, J., and Voeltz, G.K. (2011). ER Tubules Mark Sites of Mitochondrial Division. Science *334*, 358–362. https://doi.org/10.1126/science.1207385.
6. Prudent, J., Zunino, R., Sugiura, A., Mattie, S., Shore, G.C., and McBride, H.M. (2015). MAPL SUMOylation of Drp1 Stabilizes an ER/Mitochondrial Platform Required for Cell Death. Mol. Cell *59*, 941–955. https://doi.org/10.1016/j.molcel.2015.08.001.
7. Lewis, S.C., Uchiyama, L.F., and Nunnari, J. (2016). ER-mitochondria contacts couple mtDNA synthesis with mitochondrial division in human cells. Science *353*, aaf5549. https://doi.org/10.1126/science.aaf5549.
8. Hamasaki, M., Furuta, N., Matsuda, A., Nezu, A., Yamamoto, A., Fujita, N., Oomori, H., Noda, T., Haraguchi, T., Hiraoka, Y., et al. (2013).

Autophagosomes form at ER–mitochondria contact sites. Nature *495*, 389–393. https://doi.org/10.1038/nature11910.

9. Lee, K.-S., Huh, S., Lee, S., Wu, Z., Kim, A.-K., Kang, H.-Y., and Lu, B. (2018). Altered ER–mitochondria contact impacts mitochondria calcium homeostasis and contributes to neurodegeneration in vivo in disease models. Proc. Natl. Acad. Sci. USA *115*, E8844–E8853. https://doi.org/10.1073/pnas.1721136115.
10. Arruda, A.P., Pers, B.M., Parlakgül, G., Güney, E., Inouye, K., and Hotamisligil, G.S. (2014). Chronic enrichment of hepatic endoplasmic reticulum–mitochondria contact leads to mitochondrial dysfunction in obesity. Nat. Med. *20*, 1427–1435. https://doi.org/10.1038/nm.3735.
11. Çoku, J., Booth, D.M., Skoda, J., Pedrotty, M.C., Vogel, J., Liu, K., Vu, A., Carpenter, E.L., Ye, J.C., Chen, M.A., et al. (2022). Reduced ER–mitochondria connectivity promotes neuroblastoma multidrug resistance. EMBO J. *41*, e108272. https://doi.org/10.15252/embj.2021108272.
12. Thoudam, T., Ha, C.-M., Leem, J., Chanda, D., Park, J.-S., Kim, H.-J., Jeon, J.-H., Choi, Y.-K., Liangpunsakul, S., Huh, Y.H., et al. (2019). PDK4 Augments ER–Mitochondria Contact to Dampen Skeletal Muscle Insulin Signaling During Obesity. Diabetes *68*, 571–586. https://doi.org/10.2337/db18-0363.
13. Rodríguez, L.R., Calap-Quintana, P., Lapeña-Luzón, T., Pallardó, F.V., Schneuwly, S., Navarro, J.A., and Gonzalez-Cabo, P. (2020). Oxidative stress modulates rearrangement of endoplasmic reticulum-mitochondria contacts and calcium dysregulation in a Friedreich's ataxia model. Redox Biol. *37*, 101762. https://doi.org/10.1016/j.redox.2020.101762.
14. Vallese, F., Catoni, C., Cieri, D., Barazzuol, L., Ramirez, O., Calore, V., Bonora, M., Giamogante, F., Pinton, P., Brini, M., et al. (2020). An expanded palette of improved SPLICS reporters detects multiple organelle contacts in vitro and in vivo. Nat. Commun. *11*, 6069. https://doi.org/10.1038/s41467-020-19892-6.
15. Cieri, D., Vicario, M., Giacomello, M., Vallese, F., Filadi, R., Wagner, T., Pozzan, T., Pizzo, P., Scorrano, L., Brini, M., et al. (2017). SPLICS: a split green fluorescent protein-based contact site sensor for narrow and wide heterotypic organelle juxtaposition. Cell Death Differ. *25*, 1131–1145. https://doi.org/10.1038/s41418-017-0033-z.
16. Calì, T., Ottolini, D., Vicario, M., Catoni, C., Vallese, F., Cieri, D., Barazzuol, L., and Brini, M. (2019). splitGFP Technology Reveals Dose-Dependent ER-Mitochondria Interface Modulation by α-Synuclein A53T and A30P Mutants. Cells *8*, 1072. https://doi.org/10.3390/cells8091072.
17. Giamogante, F., Barazzuol, L., Poggio, E., Tromboni, M., Brini, M., and Calì, T. (2022). Stable Integration of Inducible SPLICS Reporters Enables Spatio-Temporal Analysis of Multiple Organelle Contact Sites upon Modulation of Cholesterol Traffic. Cells *11*, 1643. https://doi.org/10.3390/cells11101643.
18. Mishra, P., Carelli, V., Manfredi, G., and Chan, D.C. (2014). Proteolytic Cleavage of Opa1 Stimulates Mitochondrial Inner Membrane Fusion and Couples Fusion to Oxidative Phosphorylation. Cell Metab. *19*, 630–641. https://doi.org/10.1016/j.cmet.2014.03.011.
19. Bravo, R., Vicencio, J.M., Parra, V., Troncoso, R., Munoz, J.P., Bui, M., Quiroga, C., Rodriguez, A.E., Verdejo, H.E., Ferreira, J., et al. (2011). Increased ER–mitochondrial coupling promotes mitochondrial respiration and bioenergetics during early phases of ER stress. J. Cell Sci. *124*, 2143–2152. https://doi.org/10.1242/jcs.080762.
20. Calì, T., and Brini, M. (2021). Quantification of organelle contact sites by split-GFP-based contact site sensors (SPLICS) in living cells. Nat. Protoc. *16*, 5287–5308. https://doi.org/10.1038/s41596-021-00614-1.
21. Hertlein, V., Flores-Romero, H., Das, K.K., Fischer, S., Heunemann, M., Calleja-Felipe, M., Knafo, S., Hipp, K., Harter, K., Fitzgerald, J.C., et al. (2019). MERLIN: a novel BRET-based proximity biosensor for studying mitochondria–ER contact sites. Life Sci. Alliance *3*, e201900600. https://doi.org/10.26508/lsa.201900600.
22. Hantschel, O. (2015). Unexpected Off-Targets and Paradoxical Pathway Activation by Kinase Inhibitors. ACS Chem. Biol. *10*, 234–245. https://doi.org/10.1021/cb500886n.
23. Ciceri, P., Müller, S., O'Mahony, A., Fedorov, O., Filippakopoulos, P., Hunt, J.P., Lasater, E.A., Pallares, G., Picaud, S., Wells, C., et al. (2014). Dual kinase-bromodomain inhibitors for rationally designed polypharmacology. Nat. Chem. Biol. *10*, 305–312. https://doi.org/10.1038/nchembio.1471.
24. Kleppe, M., Koche, R., Zou, L., van Galen, P., Hill, C.E., Dong, L., De Groote, S., Papalexi, E., Hanasoge Somasundara, A.V., Cordner, K., et al. (2018). Dual Targeting of Oncogenic Activation and Inflammatory Signaling Increases Therapeutic Efficacy in Myeloproliferative Neoplasms. Cancer Cell *33*, 29–43.e7. https://doi.org/10.1016/j.ccell.2017.11.009.
25. Wernig, G., Kharas, M.G., Okabe, R., Moore, S.A., Leeman, D.S., Cullen, D.E., Gozo, M., McDowell, E.P., Levine, R.L., Doukas, J., et al. (2008). Efficacy of TG101348, a Selective JAK2 Inhibitor, in Treatment of a Murine Model of JAK2V617F-Induced Polycythemia Vera. Cancer Cell *13*, 311–320. https://doi.org/10.1016/j.ccr.2008.02.009.
26. Sakamaki, J.I., Wilkinson, S., Hahn, M., Tasdemir, N., O'Prey, J., Clark, W., Hedley, A., Nixon, C., Long, J.S., New, M., et al. (2017). Bromodomain Protein BRD4 Is a Transcriptional Repressor of Autophagy and Lysosomal Function. Mol. Cell *66*, 517–532.e9. https://doi.org/10.1016/j.molcel.2017.04.027.
27. Venkatraman, K., Lee, C.T., Garcia, G.C., Mahapatra, A., Milshteyn, D., Perkins, G., Kim, K.Y., Pasolli, H.A., Phan, S., Lippincott-Schwartz, J., et al. (2023). Cristae formation is a mechanical buckling event controlled by the inner mitochondrial membrane lipidome. EMBO J. *42*, e114054. https://doi.org/10.15252/embj.2023114054.
28. MacDonald, J.A., Bothun, A.M., Annis, S.N., Sheehan, H., Ray, S., Gao, Y., Ivanov, A.R., Khrapko, K., Tilly, J.L., and Woods, D.C. (2019). A nanoscale, multi-parametric flow cytometry-based platform to study mitochondrial heterogeneity and mitochondrial DNA dynamics. Commun. Biol. *2*, 258. https://doi.org/10.1038/s42003-019-0513-4.
29. Edington, A.R., Connor, O.M., Love, A.C., Marlar-Pavey, M., and Friedman, J.R. (2024). Functionally conserved inner mitochondrial membrane proteins CCDC51 and Mdm33 demarcate a subset of fission events. J. Cell Biol. *224*, e202403140. https://doi.org/10.1083/jcb.202403140.
30. Baik, A.H., and Jain, I.H. (2020). Turning the Oxygen Dial: Balancing the Highs and Lows. Trends Cell Biol. *30*, 516–536. https://doi.org/10.1016/j.tcb.2020.04.005.
31. Spinelli, J.B., Rosen, P.C., Sprenger, H.-G., Puszynska, A.M., Mann, J.L., Roessler, J.M., Cangelosi, A.L., Henne, A., Condon, K.J., Zhang, T., et al. (2021). Fumarate is a terminal electron acceptor in the mammalian electron transport chain. Science *374*, 1227–1237. https://doi.org/10.1126/science.abi7495.
32. Geng, J., Khaket, T.P., Pan, J., Li, W., Zhang, Y., Ping, Y., Cobos Sillero, M.I.C., and Lu, B. (2023). Deregulation of ER-mitochondria contact formation and mitochondrial calcium homeostasis mediated by VDAC in fragile X syndrome. Dev. Cell *58*, 597–615.e10. https://doi.org/10.1016/j.devcel.2023.03.002.
33. Anastasia, I., Ilacqua, N., Raimondi, A., Lemieux, P., Ghandehari-Alavijeh, R., Faure, G., Mekhedov, S.L., Williams, K.J., Caicci, F., Valle, G., et al. (2021). Mitochondria-rough-ER contacts in the liver regulate systemic lipid homeostasis. Cell Rep. *34*, 108873. https://doi.org/10.1016/j.celrep.2021.108873.
34. Hofstadter, W.A., Cook, K.C., Tsopurashvili, E., Gebauer, R., Pražák, V., Machala, E.A., Park, J.W., Grünewald, K., Quemin, E.R.J., and Cristea, I.M. (2024). Infection-induced peripheral mitochondria fission drives ER encapsulations and inter-mitochondria contacts that rescue bioenergetics. Nat. Commun. *15*, 7352. https://doi.org/10.1038/s41467-024-51680-4.
35. Poggio, E., Vallese, F., Hartel, A.J.W., Morgenstern, T.J., Kanner, S.A., Rauh, O., Giamogante, F., Barazzuol, L., Shepard, K.L., Colecraft, H.M., et al. (2023). Perturbation of the host cell Ca2+ homeostasis and ER-mitochondria contact sites by the SARS-CoV-2 structural proteins E and M. Cell Death Dis. *14*, 297. https://doi.org/10.1038/s41419-023-05817-w.

36. Filippakopoulos, P., Qi, J., Picaud, S., Shen, Y., Smith, W.B., Fedorov, O., Morse, E.M., Keates, T., Hickman, T.T., Felletar, I., et al. (2010). Selective inhibition of BET bromodomains. Nature *468*, 1067–1073. https://doi.org/10.1038/nature09504.

37. Barrow, J.J., Balsa, E., Verdeguer, F., Tavares, C.D.J., Soustek, M.S., Hollingsworth, L.R., Jedrychowski, M., Vogel, R., Paulo, J.A., Smeitink, J., et al. (2016). Bromodomain Inhibitors Correct Bioenergetic Deficiency Caused by Mitochondrial Disease Complex I Mutations. Mol. Cell *64*, 163–175. https://doi.org/10.1016/j.molcel.2016.08.023.

38. Costa-Mattioli, M., and Walter, P. (2020). The integrated stress response: From mechanism to disease. Science *368*, eaat5314. https://doi.org/10.1126/science.aat5314.

39. Kalkavan, H., Chen, M.J., Crawford, J.C., Quarato, G., Fitzgerald, P., Tait, S.W.G., Goding, C.R., and Green, D.R. (2022). Sublethal cytochrome c release generates drug-tolerant persister cells. Cell *185*, 3356–3374.e22. https://doi.org/10.1016/j.cell.2022.07.025.

40. Palchaudhuri, R., Lambrecht, M.J., Botham, R.C., Partlow, K.C., van Ham, T.J., Putt, K.S., Nguyen, L.T., Kim, S.-H., Peterson, R.T., Fan, T.M., et al. (2015). A Small Molecule that Induces Intrinsic Pathway Apoptosis with Unparalleled Speed. Cell Rep. *13*, 2027–2036. https://doi.org/10.1016/j.celrep.2015.10.042.

41. Chipuk, J.E., McStay, G.P., Bharti, A., Kuwana, T., Clarke, C.J., Siskind, L.J., Obeid, L.M., and Green, D.R. (2012). Sphingolipid Metabolism Cooperates with BAK and BAX to Promote the Mitochondrial Pathway of Apoptosis. Cell *148*, 988–1000. https://doi.org/10.1016/j.cell.2012.01.038.

42. Verfaillie, T., Rubio, N., Garg, A.D., Bultynck, G., Rizzuto, R., Decuypere, J.P., Piette, J., Linehan, C., Gupta, S., Samali, A., et al. (2012). PERK is required at the ER-mitochondrial contact sites to convey apoptosis after ROS-based ER stress. Cell Death Differ. *19*, 1880–1891. https://doi.org/10.1038/cdd.2012.74.

43. Csordás, G., Renken, C., Várnai, P., Walter, L., Weaver, D., Buttle, K.F., Balla, T., Mannella, C.A., and Hajnóczky, G. (2006). Structural and functional features and significance of the physical linkage between ER and mitochondria. J. Cell Biol. *174*, 915–921. https://doi.org/10.1083/jcb.200604016.

44. Bassot, A., Chen, J., Takahashi-Yamashiro, K., Yap, M.C., Gibhardt, C.S., Le, G.N.T., Hario, S., Nasu, Y., Moore, J., Gutiérrez, T., et al. (2023). The endoplasmic reticulum kinase PERK interacts with the oxidoreductase ERO1 to metabolically adapt mitochondria. Cell Rep. *42*, 111899. https://doi.org/10.1016/j.celrep.2022.111899.

45. Carreras-Sureda, A., Jaña, F., Urra, H., Durand, S., Mortenson, D.E., Sagredo, A., Bustos, G., Hazari, Y., Ramos-Fernández, E., Sassano, M.L., et al. (2019). Non-canonical function of IRE1α determines mitochondria-associated endoplasmic reticulum composition to control calcium transfer and bioenergetics. Nat. Cell Biol. *21*, 755–767. https://doi.org/10.1038/s41556-019-0329-y.

46. Stefely, J.A., and Pagliarini, D.J. (2017). Biochemistry of Mitochondrial Coenzyme Q Biosynthesis. Trends Biochem. Sci. *42*, 824–843. https://doi.org/10.1016/j.tibs.2017.06.008.

47. Guerra, R.M., and Pagliarini, D.J. (2023). Coenzyme Q biochemistry and biosynthesis. Trends Biochem. Sci. *48*, 463–476. https://doi.org/10.1016/j.tibs.2022.12.006.

48. Jones, M.E. (1980). Pyrimidine Nucleotide Biosynthesis in Animals: Genes, Enzymes, and Regulation of UMP Biosynthesis. Annu. Rev. Biochem. *49*, 253–279. https://doi.org/10.1146/annurev.bi.49.070180.001345.

49. Kumar, R., Landry, A.P., Guha, A., Vitvitsky, V., Lee, H.J., Seike, K., Reddy, P., Lyssiotis, C.A., and Banerjee, R. (2022). A redox cycle with complex II prioritizes sulfide quinone oxidoreductase-dependent H2S oxidation. J. Biol. Chem. *298*, 101435. https://doi.org/10.1016/j.jbc.2021.101435.

50. Mourier, A., Motori, E., Brandt, T., Lagouge, M., Atanassov, I., Galinier, A., Rappl, G., Brodesser, S., Hultenby, K., Dieterich, C., et al. (2015). Mitofusin 2 is required to maintain mitochondrial coenzyme Q levels. J. Cell Biol. *208*, 429–442. https://doi.org/10.1083/jcb.201411100.

51. Obara, C.J., Nixon-Abell, J., Moore, A.S., Riccio, F., Hoffman, D.P., Shtengel, G., Xu, C.S., Schaefer, K., Pasolli, H.A., Masson, J.-B., et al. (2024). Motion of VAPB molecules reveals ER–mitochondria contact site subdomains. Nature *626*, 169–176. https://doi.org/10.1038/s41586-023-06956-y.

52. Li, X., Gamuyao, R., Wu, M.-L., Cho, W.J., King, S.V., Petersen, R.A., Stabley, D.R., Lindow, C., Climer, L.K., Shirinifard, A., et al. (2024). A fluorogenic complementation tool kit for interrogating lipid droplet–organelle interaction. J. Cell Biol. *223*, e202311126. https://doi.org/10.1083/jcb.202311126.

53. Miner, G.E., Smith, S.Y., Showalter, W.K., So, C.M., Ragusa, J.V., Powers, A.E., Zanellati, M.C., Hsu, C.-H., Marchan, M.F., and Cohen, S. (2024). Contact-FP: A Dimerization-Dependent Fluorescent Protein Toolkit for Visualizing Membrane Contact Site Dynamics. Contact (Thousand Oaks) *7*, 25152564241228911. https://doi.org/10.1177/25152564241228911.

54. Conrad, R., and Narayan, K. (2023). Instance segmentation of mitochondria in electron microscopy images with a generalist deep learning model trained on a diverse dataset. Cell Syst. *14*, 58–71.e5. https://doi.org/10.1016/j.cels.2022.12.006.

55. Pang, Z., Lu, Y., Zhou, G., Hui, F., Xu, L., Viau, C., Spigelman, A.F., MacDonald, P.E., Wishart, D.S., Li, S., et al. (2024). MetaboAnalyst 6.0: towards a unified platform for metabolomics data processing, analysis and interpretation. Nucleic Acids Res. *52*, W398–W406. https://doi.org/10.1093/nar/gkae253.

56. Chambers, M.C., Maclean, B., Burke, R., Amodei, D., Ruderman, D.L., Neumann, S., Gatto, L., Fischer, B., Pratt, B., Egertson, J., et al. (2012). A cross-platform toolkit for mass spectrometry and proteomics. Nat. Biotechnol. *30*, 918–920. https://doi.org/10.1038/nbt.2377.

57. Tsugawa, H., Cajka, T., Kind, T., Ma, Y., Higgins, B., Ikeda, K., Kanazawa, M., VanderGheynst, J., Fiehn, O., and Arita, M. (2015). MS-DIAL: data-independent MS/MS deconvolution for comprehensive metabolome analysis. Nat. Methods *12*, 523–526. https://doi.org/10.1038/nmeth.3393.

58. Bolger, A.M., Lohse, M., and Usadel, B. (2014). Trimmomatic: a flexible trimmer for Illumina sequence data. Bioinformatics *30*, 2114–2120. https://doi.org/10.1093/bioinformatics/btu170.

59. Raney, B.J., Barber, G.P., Benet-Pagès, A., Casper, J., Clawson, H., Cline, M.S., Diekhans, M., Fischer, C., Navarro Gonzalez, J.N., Hickey, G., et al. (2024). The UCSC Genome Browser database: 2024 update. Nucleic Acids Res. *52*, D1082–D1088. https://doi.org/10.1093/nar/gkad987.

60. Zhu, L.J., Gazin, C., Lawson, N.D., Pagès, H., Lin, S.M., Lapointe, D.S., and Green, M.R. (2010). ChIPpeakAnno: a Bioconductor package to annotate ChIP-seq and ChIP-chip data. BMC Bioinform. *11*, 237. https://doi.org/10.1186/1471-2105-11-237.

61. Yu, G., Wang, L.-G., and He, Q.-Y. (2015). ChIPseeker: an R/Bioconductor package for ChIP peak annotation, comparison and visualization. Bioinformatics *31*, 2382–2383. https://doi.org/10.1093/bioinformatics/btv145.

62. Ramírez, F., Ryan, D.P., Grüning, B., Bhardwaj, V., Kilpert, F., Richter, A.S., Heyne, S., Dündar, F., and Manke, T. (2016). deepTools2: a next generation web server for deep-sequencing data analysis. Nucleic Acids Res. *44*, W160–W165. https://doi.org/10.1093/nar/gkw257.

63. Williams, R.T., Guarecuco, R., Gates, L.A., Barrows, D., Passarelli, M.C., Carey, B., Baudrier, L., Jeewajee, S., La, K., Prizer, B., et al. (2020). ZBTB1 Regulates Asparagine Synthesis and Leukemia Cell Response to L-Asparaginase. Cell Metab. *31*, 852–861.e6. https://doi.org/10.1016/j.cmet.2020.03.008.

64. Chan, S.W., and Chen, J.Z. (2009). Measuring mtDNA damage using a supercoiling-sensitive qPCR approach. Methods Mol. Biol. *554*, 183–197. https://doi.org/10.1007/978-1-59745-521-3_12.

65. Kukulski, W., Schorb, M., Welsch, S., Picco, A., Kaksonen, M., and Briggs, J.A.G. (2012). Precise, Correlated Fluorescence Microscopy and Electron Tomography of Lowicryl Sections Using Fluorescent Fiducial Markers. Chapter 13. Methods Cell Biol. *111*, 235–257. https://doi.org/10.1016/b978-0-12-416026-2.00013-3.

66. Kremer, J.R., Mastronarde, D.N., and McIntosh, J.R. (1996). Computer Visualization of Three-Dimensional Image Data Using IMOD. J. Struct. Biol. *116*, 71–76. https://doi.org/10.1006/jsbi.1996.0013.

67. Paul-Gilloteaux, P., Heiligenstein, X., Belle, M., Domart, M.-C., Larijani, B., Collinson, L., Raposo, G., and Salamero, J. (2017). eC-CLEM: flexible multidimensional registration software for correlative microscopies. Nat. Methods *14*, 102–103. https://doi.org/10.1038/nmeth.4170.

68. de Chaumont, F., Dallongeville, S., Chenouard, N., Hervé, N., Pop, S., Provoost, T., Meas-Yedid, V., Pankajakshan, P., Lecomte, T., Le Montagner, Y.L., et al. (2012). Icy: an open bioimage informatics platform for extended reproducible research. Nat. Methods *9*, 690–696. https://doi.org/10.1038/nmeth.2075.

69. Xu, C.S., Hayworth, K.J., Lu, Z., Grob, P., Hassan, A.M., García-Cerdán, J.G., Niyogi, K.K., Nogales, E., Weinberg, R.J., and Hess, H.F. (2017). Enhanced FIB-SEM systems for large-volume 3D imaging. eLife *6*, e25916. https://doi.org/10.7554/elife.25916.

70. Lowe, D.G. (2004). Distinctive Image Features from Scale-Invariant Keypoints. Int. J. Comput. Vis. *60*, 91–110. https://doi.org/10.1023/b:visi.0000029664.99615.94.

71. Hoffman, D.P., Shtengel, G., Xu, C.S., Campbell, K.R., Freeman, M., Wang, L., Milkie, D.E., Pasolli, H.A., Iyer, N., Bogovic, J.A., et al. (2020). Correlative three-dimensional super-resolution and block-face electron microscopy of whole vitreously frozen cells. Science *367*, eaaz5357. https://doi.org/10.1126/science.aaz5357.

72. Bharathan, N.K., Giang, W., Hoffman, C.L., Aaron, J.S., Khuon, S., Chew, T.-L., Preibisch, S., Trautman, E.T., Heinrich, L., Bogovic, J., et al. (2023). Architecture and dynamics of a desmosome–endoplasmic reticulum complex. Nat. Cell Biol. *25*, 823–835. https://doi.org/10.1038/s41556-023-01154-4.

73. Bielawski, J., Pierce, J.S., Snider, J., Rembiesa, B., Szulc, Z.M., and Bielawska, A. (2009). Lipidomics. Methods Mol. Biol. *579*, 443–467. https://doi.org/10.1007/978-1-60761-322-0_22.

74. Kind, T., Liu, K.-H., Lee, D.Y., DeFelice, B., Meissen, J.K., and Fiehn, O. (2013). LipidBlast in silico tandem mass spectrometry database for lipid identification. Nat. Methods *10*, 755–758. https://doi.org/10.1038/nmeth.2551.

75. Tsugawa, H., Ikeda, K., Takahashi, M., Satoh, A., Mori, Y., Uchino, H., Okahashi, N., Yamada, Y., Tada, I., Bonini, P., et al. (2020). A lipidome atlas in MS-DIAL 4. Nat. Biotechnol. *38*, 1159–1163. https://doi.org/10.1038/s41587-020-0531-2.

76. Burger, N., Logan, A., Prime, T.A., Mottahedin, A., Caldwell, S.T., Krieg, T., Hartley, R.C., James, A.M., and Murphy, M.P. (2020). A sensitive mass spectrometric assay for mitochondrial CoQ pool redox state in vivo. Free Radic. Biol. Med. *147*, 37–47. https://doi.org/10.1016/j.freeradbiomed.2019.11.028.

77. Liu, X., Gygi, S.P., and Paulo, J.A. (2021). A Semiautomated Paramagnetic Bead-Based Platform for Isobaric Tag Sample Preparation. J. Am. Soc. Mass Spectrom. *32*, 1519–1529. https://doi.org/10.1021/jasms.1c00077.

78. Huttlin, E.L., Jedrychowski, M.P., Elias, J.E., Goswami, T., Rad, R., Beausoleil, S.A., Villén, J., Haas, W., Sowa, M.E., and Gygi, S.P. (2010). A Tissue-Specific Atlas of Mouse Protein Phosphorylation and Expression. Cell *143*, 1174–1189. https://doi.org/10.1016/j.cell.2010.12.001.

79. Li, H., and Durbin, R. (2009). Fast and accurate short read alignment with Burrows–Wheeler transform. Bioinformatics *25*, 1754–1760. https://doi.org/10.1093/bioinformatics/btp324.

80. Zhang, Y., Liu, T., Meyer, C.A., Eeckhoute, J., Johnson, D.S., Bernstein, B.E., Nusbaum, C., Myers, R.M., Brown, M., Li, W., et al. (2008). Model-based Analysis of ChIP-Seq (MACS). Genome Biol. *9*, R137. https://doi.org/10.1186/gb-2008-9-9-r137.

81. Paulsen, M.T., Veloso, A., Prasad, J., Bedi, K., Ljungman, E.A., Magnuson, B., Wilson, T.E., and Ljungman, M. (2014). Use of Bru-Seq and BruChase-Seq for genome-wide assessment of the synthesis and stability of RNA. Methods *67*, 45–54. https://doi.org/10.1016/j.ymeth.2013.08.015.

82. McShane, A., Narayanan, I.V., Paulsen, M.T., Ashaka, M., Blinkiewicz, H., Yang, N.T., Magnuson, B., Bedi, K., Wilson, T.E., and Ljungman, M. (2024). Characterizing nascent transcription patterns of PROMPTs, eRNAs, and readthrough transcripts in the ENCODE4 deeply profiled cell lines. Preprint at bioRxiv. https://doi.org/10.1101/2024.04.09.588612.

STAR★METHODS

KEY RESOURCES TABLE

REAGENT or RESOURCE	SOURCE	IDENTIFIER
Antibodies		
Vinculin (clone E1E9V)	Cell Signaling Technology	Cat#13901; RRID: AB_2728768
MFN2 (clone D2D10)	Cell Signaling Technology	Cat#9482; RRID: AB_2716838
DRP1 (clone D6C7)	Cell Signaling Technology	Cat#8570; RRID: AB_10950498
Phospho-DRP1 S616	Cell Signaling Technology	Cat#3455; RRID: AB_2085352
Phospho-DRP1 S637	Cell Signaling Technology	Cat#4867; RRID: AB_10622027
Mitofilin/MIC60	Proteintech	Cat#10179-1-AP; RRID: AB_2127193
MIC25/CHCHD6	Proteintech	Cat#20639-1-AP; RRID: AB_10697667
RTN4/NOGO	Proteintech	Cat#10740-1-AP; RRID: AB_2183598
COQ9	Proteintech	Cat#14874-1-AP; RRID: AB_2082218
CLIMP63/CKAP4	Enzo Life Sciences	Cat#ENZ-ABS669-0100; RRID: AB_2276276
OPA1	Cell Signaling Technology	Cat#80471; RRID: AB_2734117
ATF4	Cell Signaling Technology	Cat#97038; RRID: AB_3698388
eIF2a	Cell Signaling Technology	Cat#9722; RRID: AB_2230924
Phospho-eIF2a S51	Cell Signaling Technology	Cat#9721; RRID: AB_330951
BiP/HSPA5	Cell Signaling Technology	Cat#3177; RRID: AB_2119845
CHOP/DDIT3	Cell Signaling Technology	Cat#2895; RRID: AB_2089254
BRD4	Cell Signaling Technology	Cat#13440; RRID: AB_2687578
BRD4 ChIP-Seq Antibody	Diagenode	C15410337
BRD4 (chromatin fractionation)	Bethyl Laboratories	Cat#BL-149-2H5; RRID: AB_2631885
c-MYC	Cell Signaling Technology	Cat#18583; RRID: AB_2895543
STAT3	Cell Signaling Technology	Cat#9139; RRID: AB_331757
Phospho-STAT3 Y705	Cell Signaling Technology	Cat#9145; RRID: AB_2491009
IP3R-I/II/III	Santa Cruz Biotechnology	Cat#SC-377518; RRID: AB_2637028
TOM20	Cell Signaling Technology	Cat#42406; RRID: AB_2687663
CCPG1	Cell Signaling Technology	Cat#80158; RRID: AB_2935809
PERK	Cell Signaling Technology	Cat#3192; RRID: AB_2095847
IRE1α	Cell Signaling Technology	Cat#3294; RRID: AB_823545
ATF6	Cell Signaling Technology	Cat#65880; RRID: AB_2799696
XBP1s	Cell Signaling Technology	Cat#40435; RRID: AB_2891025
LC3B	Cell Signaling Technology	Cat#3868; RRID: AB_2137707
HIF1α	Cell Signaling Technology	Cat#14179; RRID: AB_2622225
JAK2	Cell Signaling Technology	Cat#3230; RRID: AB_2128522
Flag (DYKDDDDK)	Cell Signaling Technology	Cat#14793; RRID: AB_2572291
GFP	Proteintech	50430-2-AP; RRID: AB_11042881
Total OXPHOS Human WB Antibody Cocktail	Abcam	ab110411; RRID: AB_2756818
Chemicals, peptides, and recombinant proteins		
Fedratinib	MedChem Express	Cat#HY-10309
Thapsigargin	Cayman Chemicals	Cat#10522
Ruxolitinib	Cayman Chemicals	Cat#11609
dBET6	Cayman Chemicals	Cat#35385
JQ1	Cayman Chemicals	Cat#11187
Actinomycin D	Cayman Chemicals	Cat#11421

(*Continued on next page*)

Continued

REAGENT or RESOURCE	SOURCE	IDENTIFIER
AS-2863619	Cayman Chemicals	Cat#30976
NVP2	Cayman Chemicals	Cat#34725
Piericidin A	Cayman Chemicals	Cat#15379
TTFA	Cayman Chemicals	Cat#15517
Antimycin A	Cayman Chemicals	Cat#34799
Myxothiazol	Sigma Aldrich	Cat#T5580
Oligomycin	Cayman Chemicals	Cat#11341
CCCP	Cayman Chemicals	Cat#25458
FG4592	Cayman Chemicals	Cat#15294
MitoPQ	Cayman Chemicals	Cat#18808
S3QEL2	Cayman Chemicals	Cat#18556
Z-VAD-FMK	Cayman Chemicals	Cat#14463
PKR-IN-C16	MedChem Express	Cat#HY-13977A
Gamitrinib TPP hexafluorophosphate (GTPP)	MedChem Express	HY-102007A
ISRIB	Sigma Aldrich	SML0843
BEPP	Sigma Aldrich	B2938
CCT020312	Cayman Chemicals	Cat#36577
Histinidol	Cayman Chemicals	Cat#18739
BTdCPU	Fisher Scientific	32-489-210MG
Salubrinal	Cayman Chemicasl	Cat#14735
Chloroquine	Selleck Chemicals	S4157
Bafilomycin A1	Selleck Chemicals	S1413
Tauroursodeoxycholic acid (TUDCA)	Cayman Chemicals	20277
Doxycycline (hyclate)	Cayman Chemicals	14422
10074-G5	Cayman Chemicals	Cat#17408
10058-F4	Cayman Chemicals	Cat#15929
Mito paraquat (MitoPQ)	Selleck Chemicals	E1252
CGP37157 (NCLXi)	Cayman Chemicals	Cat#15611
BATPA-AM	Cayman Chemicals	Cat#15551
Ru360 (MCUi)	EMD Millipore	557440
tert-Butyl hydroperoxide (TBHP)	Thermo Scientific Chemicals	180342500
Critical commercial assays		
Seahorse Mito Stress Test	Agilent Technologies	103015–100
Duolink® In Situ Detection Reagents FarRed	Sigma Aldrich	DUO92013
iDeal ChIP-seq kit for Transcription Factors	Diagenode	C01010055
IPure Kit V2	Diagenode	C03010015
RNeasy Mini	Qiagen	74104
Stains and dyes		
Mitotracker Deep Red FM	Invitrogen	M22426
MitoTracker Green	Invitrogen	M7514
MitoSOX Deep Red	Dojindo	MT1412
Tetramethylrhodamine, Ethyl Ester Perchlorate (TMRE)	Invitrogen	T669
Rhod-2 AM	Invitrogen	R1244
MitoBrilliant 646	Tocris Bioscience	7700

(*Continued on next page*)

Continued

REAGENT or RESOURCE	SOURCE	IDENTIFIER
DAPRed	Dojindo	D677-10
Hoechst 3342	Invitrogen	cat#H3570
Lysotracker Deep Red	Invitrogen	cat#L12492
JF646	Promega	GA11520
HCS CellMask Deep Red Stain	Invitrogen	cat#H32721
Experimental models: Cell lines		
SW480	ATCC	CCL-228
HT1080	ATCC	CCL-121
HCT116	ATCC	CCL-247
DLD1	ATCC	CCL-221
HeLa	ATCC	CCL-2
U2OS	ATCC	HTB-96
HEK293T	ATCC	CRL-3216
Jurkat	ATCC	TIB-152
K562	ATCC	CCL-243
B16-F0	ATCC	CRL-6322
A549	ATCC	CCL-185
PA-TU8902	This study	N/A
KPC7940	This study	N/A
Recombinant DNA		
SPLICS ER–mitochondria reporter constructs	Giamogante, F. et al.[17]	N/A
mKate contact site control constructs	Cali, T. and Brini, M.[20]	N/A
pCW57.1_AOX-FLAG	Addgene	Plasmid #177984
pclbw-mitoTagRFP	Addgene	Plasmid #58425
lentiCRISPR-v2	Addgene	Plasmid #52961
pLV hU6-sgRNA hUbC-dCas9-KRAB-T2a-Puro	Addgene	Plasmid #71236
BFP ER–mitochondria tether	VectorBuilder	N/A
CMV-VSV-G	Addgene	Plasmid #8454
psPAX2	Addgene	Plasmid #12260
Halo-Sec61-C-18	Addgene	Plasmid #123285
siRNAs, sgRNAs, and primers	This Study	Table S7
Software and algorithms		
ImageJ/Fiji	NIH	https://imagej.net/ij/
clusterProfiler v4.2.2 (R package)	Bioconductor	https://bioconductor.org/packages/release/bioc/html/clusterProfiler.html
FlowJo	BD Biosciences	https://www.flowjo.com/
Seahorse Wave	Agilent	https://www.agilent.com/en/product/cell-analysis/real-time-cell-metabolic-analysis/xf-software/seahorse-wave-desktop-software-740897?srsltid=AfmBOoqHwcOeY-o13LlQsIvcTq25DftSvmvyFhpBE-3yZVahZmWbtLvl
Prism v 10.6.1	GraphPad	https://www.graphpad.com/
SITF algorithm	https://github.com/gleb-shtengel/FIBSEM_gs_py	N/A
N2V2 algorithm	https://github.com/juglab/n2v	N/A
Empanada	Conrad and Narayan[54]	https://empanada.readthedocs.io/en/stable/
MassHunter Quantitative Analysis Software	Agilent	https://www.agilent.com/en/product/software-informatics/mass-spectrometry-software/data-analysis/quantitative-analysis

(*Continued on next page*)

Continued

REAGENT or RESOURCE	SOURCE	IDENTIFIER
MetaboAnalyst 6.0	Pang, Z. et al.[55]	https://www.metaboanalyst.ca/
Proteowizard msconvert	Chambers, M.C. et al.[56]	https://proteowizard.sourceforge.io/
MS-DIAL	Tsugawa, H. et al.[57]	https://systemsomicslab.github.io/compms/msdial/main.html
TraceFinder 5.1	Thermo Fisher Scientific	https://www.thermofisher.com/us/en/home/industrial/mass-spectrometry/liquid-chromatography-mass-spectrometry-lc-ms/lc-ms-software/lc-ms-data-acquisition-software/tracefinder-software.html
Trimmomatic v 0.39	Bolger, A.M. et al.[58]	https://github.com/usadellab/Trimmomatic
UCSC Genome Browser	Raney, B.J. et al.[59]	https://genome.ucsc.edu/
ChipPeakAnno v3.0.0	Zhu, L.J. et al.[60]	https://bioconductor.org/packages/release/bioc/html/ChIPpeakAnno.html
ChipSeeker v1.29.1	Yu, G. et al.[61]	https://bioconductor.org/packages/release/bioc/html/ChIPseeker.html
deepTools	Ramirez, F. et al.[62]	https://deeptools.readthedocs.io/en/latest/
Adobe Illustrator 2025	Adobe	https://www.adobe.com/products/illustrator/campaign/pricing.html?sdid=ZFN4FBV5&mv=search&mv2=paidsearch&ef_id=Cj0KCQiAo4TKBhDRARIsAGW29bcTgq5kBtJQLfE4WWIi_lwX06T0_XntqsyqhBOWGkUXNCkp_e5kUPcaAlWQEALw_wcB:G:s&s_kwcid=AL!3085!3!356518781936!e!!g!!adobe%20illustrator!1711729586!70905759510&gad_source=1&gad_campaignid=1711729586&gbraid=0AAAAAD5r4AxFICF7pf5RVxLXebfjRmJt9&gclid=Cj0KCQiAo4TKBhDRARIsAGW29bcTgq5kBtJQLfE4WWIi_lwX06T0_XntqsyqhBOWGkUXNCkp_e5kUPcaAlWQEALw_wcB
Biorender	Biorender	https://www.biorender.com/
Deposited data		
Source data and supplementary movies	This study	Mendeley Data: https://doi.org/10.17632/jc6wr2bry3.1
Image based drug repurposing screen code and data availability	This study	Zenodo: https://doi.org/10.5281/zenodo.13963526
ProteomeXchange Proteomics data	This study	PRIDE partner repository: PXD056917
Bru-Seq data	This Study	NCBI GEO: GSE278077
ChIP-Seq data	This Study	NCBI GEO: GSE280900

EXPERIMENTAL MODEL AND STUDY PARTICIPANT DETAILS

Generation of SPLICS stable cell lines

The SPLICS reporter is composed of a split GFP_{1-10} barrel localized to the mitochondrial outer membrane, a P2A self-cleavage signal for equimolar expression, and the remaining $beta_{11}$ fragment targeted to the ER membrane. Upon ERMCS formation within the 8–10 nm distance, the split-GFP reporter forms intact GFP. Doxycycline-inducible SPLICS reporter stable cell lines were generated via a three-plasmid PiggyBac transposase system. Cells were co-transfected with the plasmids (hyPBase, SPLICS ER-MT Short, and neomycin resistance plasmids provided by Tito Calì[17] and available upon request) using Lipofectamine 2000 transfection reagent, then the next day selected with 2 mg/ml of G418 (geneticin) for 7 days. After selection, 100 ng/ml of doxycycline were used to induce reporter expression, and GFP positive cells were sorted on BigFoot Spectral Cell Sorter (Invitrogen) to isolate GFP positive isogenic clones. Clones were cultured and screened for accurate localization of SPLICS reporter to mitochondria and ER via live cell imaging and for normal mitochondrial oxygen consumption rate. For ERMCS analysis with SPLICS, cells will be induced with 100 ng/ml of doxycycline for minimally 24 hr before treatment or analysis. SW480 and HT1080 SPLICS clones were then transduced with lentivirus carrying pclbw-mitoTagRFP (see following section) using 10 μg/mL polybrene and incubated for 48 hours. GFP/RFP double positive cells were then sorted on the BigFoot Spectral Cell Sorter (Invitrogen) to isolate GFP/RFP double positive isogenic clones. All experiments throughout the manuscript were performed with the same isogenic clones of SW480 and HT1080 SPLICS/mitotagRFP reporter cells unless otherwise mentioned.

Generation of genetically modified cell lines

sgRNAs (oligonucleotide sequences are indicated in Table S7) were ligated into BsmBI-linearized lentiCRISPR-v2 (for CRISPR KO) or pLV hU6-sgRNA hUbC-dCas9-KRAB-T2a-Puro (pLV hU6-sgRNA hUbC-dCas9-KRAB-T2a-Puro was a gift from Charles Gersbach (Addgene plasmid # 71236; http://n2t.net/addgene:71236; RRID:Addgene_71236)) with T4 ligase (NEB). AOX overexpression plasmid was achieved with pCW57.1_AOX-FLAG (pCW57.1_AOX-FLAG was a gift from David Sabatini & Jessica Spinelli (Addgene plasmid # 177984; http://n2t.net/addgene:177984; RRID:Addgene_177984)). MitoTagRFP plasmid was acquired from Addgene (pclbw-mitoTagRFP was a gift from David Chan (Addgene plasmid # 58425; http://n2t.net/addgene:58425; RRID:Addgene_58425). BFP and BFP-ER-mitochondria tether were generated via Vectorbuilder (pLV[Exp]-Bsd-CMV>{new mTagBFP2} and pLV[Exp]-Bsd-CMV>{new mTagBFP2 ER mito tether}). Lentiviral vectors expressing sgRNAs were transfected into HEK293T cells with lentiviral packaging vectors CMV VSV-G and psPAX2 using XtremeGene 9 transfection reagent (Roche). After 24 h, media was aspirated and replaced by fresh media. The virus-containing supernatant was collected 48 h after transfection and filtered using a 0.45 mm filter to eliminate cells. Cells to be transduced were plated in 6-well tissue culture plates and infected in media containing virus and 8 μg/mL of polybrene. Cells were spin infected by centrifugation at 1,100 g for 1.5 h. After transduction, media was changed, and cells were selected with puromycin (for sgRNA lentiviral vector) for 72 hrs.

Cell culture

HT1080, SW480 HCT116, DLD1, SW480, HeLa, U2OS, A459, PA-TU8902, K562, Jurkat, B16, KPC7940 cells were maintained at 37°C in 5% CO_2 and 21% O_2. HT1080, SW480 HCT116, DLD1, SW480, HeLa, U2OS, A459, PA-TU8902, B16 and KPC7940 cells were cultured in Dulbecco's Modified eagle Medium (DMEM) supplemented with 10% FBS and 1% antibiotic/antimycotic, whereas Jurkat and K562 cells were cultured in Roswell Park Memorial Institute (RPMI) supplemented with 10% FBS and 1% antibiotic/antimycotic.

METHOD DETAILS

siRNA mediated knockdown

siRNAs for BRD4 were transfected using a reverse transfection protocol and Lipofectamine RNAiMAX. siRNA was purchased from Horizon Discovery with the following information: siGENOME Human BRD4 (23476) siRNA – SmartPool, 5 nmol.

Western Blots

Whole-cell lysate preparations were described previously (Anderson et al., 2013). Whole cell lysates were prepared from cell lines by RIPA buffer. Homogenates were incubated in RIPA buffer for 15 min on ice followed by 13,000 rpm centrifugation for 15 min. Supernatants were transferred to a new tube and mixed with 5× Laemmli buffer and boiled for 5 min. Lysates containing 30–40 μg of protein per well were separated by SDS-PAGE, transferred onto nitrocellulose membranes, and immunoblotted overnight at 4°C with indicated antibodies. All the primary antibodies were used at a dilution of 1:1000. HRP-conjugated secondary antibodies used were anti-rabbit and anti-mouse at a dilution of 1: 2000 and immunoblots were developed using the iBright Imaging System and iBright Analysis Software (Thermofisher).

CRISPR Screen

For the epigenetics library screen in SW480 reporter cells, the human sgRNA library was described in this paper[63] was used. The titer of lentiviral supernatants was determined by infecting targets cells at several amounts of virus in the presence of polybrene (10 μg/mL), counting the number of drug resistant infected cells after 3 days of selection. 40 million target cells were infected at an MOI of ~0.5 and selected with puromycin (1 ug/mL) 72 h after infection. An initial pool of 30 million cells was harvested for genomic DNA extraction. The remaining cells were cultured for 6 days, treated with fedratinib for 24 hr, then 25 million cells were sorted from the top and bottom 10% of SPLICS/mitoTagRFP fluorescent ratio on day 8. After which cells were harvested for genomic DNA extraction. sgRNA inserts were PCR amplified (primers listed in Table S7, purified and sequenced on a NextSeq (Illumina). Sequencing reads were mapped and the abundance of each sgRNA was tallied. Gene score is defined as the median log2 fold change in the abundance between the initial and final population of all sgRNAs targeting that gene. Full result of the screen with sequencing primers can be found in the supplemental data.

CRISPR screen analysis

sgRNA read counts were generated by aligning sequencing reads to the sgRNA library sequences, with only exact matches allowed. sgRNA abundances were calculated for both sorted populations by first adding a pseudocount of 1, then dividing by the total number of reads in each given sample. For each sgRNA, a differential score was calculated as the log2 fold-change in sgRNA abundance between the GFP-high (top 10%) and GFP-low (bottom 10%) cell populations. Gene level differential scores were generated by taking the mean score of all sgRNAs targeting the same gene. The set of differential gene scores was then standardized by subtracting the mean from each gene score then dividing by the standard deviation (Z-score).

Gene set enrichment analysis (GSEA) for CRISPR screen and proteomics

Gene set enrichment analysis was performed on the set of standardized differential gene scores using the clusterProfiler (v4.2.2) package in R. The gseGO() function was called on the data using all ontologies, min and max GSSsizes set to 10 and 500, respectively, FDR as the p-adjustment method, and an FDR cutoff of 0.01.

Imaging based drug repurposing screen

384-well, black, optically clear flat-bottom, tissue-culture treated plates (Perkin – Elmer cat# 6057302) were coated with 0.1mg/ml of poly-D-lysine hydrobromide (Sigma-Aldrich cat# P6407-5MG) at 37°C for 1hr. Then each plate is washed with molecular grade sterile water once, and then dried at room temperature for 1 hr. Each plate was then dry-spotted with 50nL of 2mM drug solution in DMSO using a Beckman Echo 650 acoustic liquid handler. In each plate, we have 2 columns of vehicle control (dimethylsulfoxide/DMSO) and 2 columns of thapsigargin (50 nM) as positive control for inducing endoplasmic reticulum-mitochondrial contact sites. With the plates coated and dry-spotted with drugs, 5000 SW480 colorectal cancer cells were plated in each well with complete DMEM media with a final drug concentration at 2μM. After incubation with the drug for 24 hr, cells were washed with PBS 3 times then fixed with 4% paraformaldehyde (PFA) in 1x PBS (Thermofisher, cat#043368.9M) at room temperature for 15 min in the dark. PFA was removed with 3 PBS washes and the fixed cells were staining with Hoechst 33342 (Invitrogen, cat# H3570, final concentration: 5 μg/ml) and HCS CellMask Deep Red Stain (Invitrogen, cat# H32721, final concentration: 1 μg/ml) for 1 hr at 37°C for 1hr. After staining, the cells were washed with PBS 3 times, and were left in PBS in the dark at 4°C until imaging. Plates were imaged on a Yokogawa CellVoyager 8000 using a 40X/1.0NA water immersion objective lens and nine fields per well were imaged across three channels to visualize Hoechst, GFP, Mitotag RFP and HCS CellMask Deep Red. Cellpose was used to identify nuclei and a custom CellProfiler pipeline was used to delineate the whole cell, mitochondria, GFP spots and per-cell feature extraction was performed. Endoplasmic reticulum–mitochondria contact sites (ERMCS) were identified by counting GFP spots within the cell. A XGBoost machine learning model was trained on centered/scaled cell-level features trained against the negative control (DMSO) and thapsigargin treated positive control wells to enable hit picking. XGBoost models were trained on the screening data controls from the entire screen with an 80%/20% train/test split. Model performance was excellent with a R2>0.95. Z-prime factors were calculated for each plate and plates below 0.5 were rejected and re-screened. High correlation was found between the XGBoost score and the GFP spot count per-cell, however, the XGBoost score exhibited significantly higher separation between the controls and led to higher Z-primes.

A liberal hit threshold of 3 standard deviations above the mean of the negative control ($\mu+3\sigma$) was used to maximize hit detection despite an increase in the false positive rate. False positives were eliminated in dose-response confirmation where 64 compounds were tested in 10-point:2-fold dilution from 10uM to 20nM in triplicate wells. Of the 64 compounds tested, 33 were found to be dose-responsive (52% confirmation rate). This is typical for a bioactive compound library where the compound potencies range from sub-nanomolar to micromolar range and, often, potent hits are obscured by cytotoxicity when screening at low micromolar concentrations. Hits were cherry picked and confirmed with triplicate 10-point/2-fold dilution and EC50 values were fit. Images and details of the screen were deposited to Zenodo and are publicly available in the repository as part of this record: 10.5281/zenodo.13963526.

Oxygen Consumption Rate (Seahorse)

Cells were seeded at 2 × 104 cells/well in 80 μl/well of normal growth media (DMEM with 25 mM Glucose and 2 mM Glutamine) in an Agilent XF96 V3 PS Cell Culture Microplate (#101085-004). To achieve an even distribution of cells within wells, plates were incubated on the bench top at room temperature for 1 h before incubating at 37 °C, 5% CO2 overnight. To hydrate the XF96 FluxPak (#102416-100), 200 μL/well of sterile water was added and the entire cartridge was incubated at 37 °C, no CO2 overnight. The following day, 1 h prior to running the assay, 60 μL/well of growth media was removed from the cell culture plate, and cells were washed twice with 200 μL/well of assay medium (XF DMEM Base Medium, pH 7.4 (#103575-100) containing 25 mM glucose (#103577-100) and 2 mM glutamine (#103579-100)). After washing, 160 μL/well of assay medium was added to the cell culture plate for a final volume of 180 μL/well. Cells were then incubated at 37 °C, without CO2 until analysis. One hour prior to the assay, water from the FluxPak hydration was exchanged for 200 μL/well of XF Calibrant (#100840-000) and the cartridge was returned at 37 °C, without CO2 until analysis. Oligomycin (100 μM), FCCP (100 μM), and Rotenone/Antimycin (50 μM) from the XF Cell Mito Stress Test Kit (#103015-100) were re-constituted in assay medium to make the indicated stock concentrations. Twenty microliters of Oligomycin was loaded into Port A for each well of the FluxPak, 22 μL of FCCP into Port B, and 25 μL of Rotenone/Antimycin into Port C. Port D was left empty. The final FCCP concentration was optimized to achieve maximal respiration in each condition. The Mito Stress Test was conducted on an XF96 Extracellular Flux Analyzer and OCR was analyzed using Wave 2.6 software. Following the assay, OCR was normalized to cell number utilizing Agilent Cytation5 live cell imaging with Gen5 software.

MT-DNA Quantification

Cells were pelleted, washed 1X in PBS, and then lysed in buffer (25 mM NaOH, 0.2 mM EDTA) for 15 minutes at 95°C. Lysis was neutralized with buffer (40 mM Tris-HCl) and centrifuged at 16,000 x g for 10 minutes at 4°C. Supernatant containing MT-DNA was quantified on with nanodrop. Primers amplifying the MT-DNA marker D-Loop and the nuclear DNA marker β-Globin were used and the relative MT-DNA to nuclear DNA was quantified in each sample.[64]

Mitochondria isolation

SW480 and HT1080 cells were scraped and pelleted at 1000 x g for 5 minutes. Cell pellets were washed in 1X PBS and pelleted at 1000 x g for 5 minutes. Cells were re-suspended in isolation buffer (200 mM sucrose, 10 mM Tris HCl, 1 mM EGTA/Tris, pH 7.4 (adjusted with 1M HEPES)), transferred into a 27-gauge needle and homogenized by 10 repeated resuspensions. Homogenates were transferred into tubes and spun at 600 x g for 10 minutes at 4°C. Supernatants were moved to a new tube and centrifugation was repeated. Then, supernatants were moved to a new tube and pelleted at 7,000 x g for 10 minutes at 4°C. Pellets were washed in isolation buffer and centrifugation was repeated two more times. For biochemical analyses, mitochondria were aliquoted in 50 μg pellets.

Flow cytometry for cells

HT1080 and SW480 cells were seeded 48 hr to 72 hr prior to the experiment at 50K and 75K cells density to achieve final 70% confluency by the time of analysis. For analyzing SPLICS and mitoTagRFP intensity, cells were washed, trypsinized, and filtered through a cell strainer prior to analyzing. For MitoSOX Deep Red(Dojindo, cat#: MT14-12), MitoTracker Green (Invitrogen, cat#: M7514), Tetramethylrhodamine, Ethyl Ester, Perchlorate/TMRE (Invitrogen, cat#: T669), and Rhod-2, AM (Invitrogen, cat#: R1244) experiments, cells were stained with 1 μM of MitoSOX Deep Red, 100 nM of MitoTracker Green, 500 nM of TMRE, 10μM of DAPRed (stained for 30 minutes, and then gets replaced in regular media) and 5μM of Rhod-2 for 30 min 37 °C, washed twice with warm PBS, and proceeded with the same processing procedure as unstained cells. Fluorescence activated cell sorting (FACS) was performed on Bigfoot Spectral Cell Sorter (Invitrogen), in which the fluorescence intensity of minimum 10K individual cells was quantified in their specific channel. Data were analyzed using FlowJo software (TreeStar).

Fluorescence activated mitochondria sorting (FAMS) and analysis

SW480 and HT1080 SPLICS/mitoTagRFP-expressing cells are plated at $3e^6$ and $6e^6$ respectively in a 150-mm plate 48 hours before sorting with doxycycline treatment to induce SPLICS expression. Cells were treated with fedratinib or vehicle (DMSO) control overnight. The next morning, cells were stained with MitoBrilliant 646 (Tocris #7700) at 200 nM for 1 hour prior to mitochondrial isolation. For control experiments, cells were treated with 25 μM CCCP for 1 hour prior to staining with 50 nM MitoTracker Deep Red FM (Invitrogen M22426) for 1 hour or overnight with 50 μM CGP-37157 followed by 5 μM Rhod-2 AM (Invitrogen, cat#: R1244) for 30 minutes. Mitochondria isolations were conducted as previously indicated. FAMS was conducted on the BigFoot Spectral Cell Sorter (Invitrogen) with 70-micron nozzle. The fluidics were flushed with deionized water for 5 minutes followed by equilibration with mitochondrial isolation buffer for another 5 minutes. Polystyrene beads (Spherotech) with defined sizes (0.2 μm, 0.5 μm, 1 μm, and 2 μm) from were used to determine gating size of mitochondria particles. After gating for size, mitochondria populations were determined using mitoTagRFP and MitoBrilliant 646 double positive gates. The populations then were analyzed based on GFP signal. $SPLICS^{Lo}$ mitochondria are determined based on vehicle control, and $SPLICS^{Hi}$ mitochondria are separated based on the formation of distinct GFP population in fedratinib-treated cells. For proteomics, contain 60 million mitochondria were sorted in each condition and four replicates were collected.

Live cell confocal imaging

35mm glass bottom plates (Ibidi) were coated with 0.1mg/ml of poly-D-Lysine (Sigma) for 1 hour at 37°C, washed once with sterile water, dry in the biosafety cabinet for 2 hours, and then complete media was added on to equilibrate for 20 min in the incubator. 50K of HT1080 and 100K of SW480 cells were then plated to achieve final 60-70% confluency by the time of imaging. Cells with HaloTag-Sec61 were stained with 200nM of JaneliaFluor 646 (JF646, Promega) for 30min at 37°C, and then washed once with warm PBS. Cells were counterstained with 2000x dilution of Hoechst 33342 (Thermofisher) for 15min at 37°C. FluoroBrite DMEM was used as the media for live cell imaging. The cells were imaged using Zeiss LSM 980 Airyscan 2 microscope and detector equipped with a 63x oil objective with a 1.4 numerical aperture. CO_2 and humidity was equilibrated for at least 30 min before imaging. Post-processing was done with Zen 3.4 (Blue edition).

Immunofluorescence (IF)

Number 1.5 round 10-mm glass coverslips were coated with 0.1mg/ml of poly-D-Lysine (Sigma) for 1 hour at 37°C, washed once with sterile water, dry in the biosafety cabinet for 2 hours, and then complete media was added on to equilibrate for 20 min in the incubator. 50K of HT1080 and 100K of SW480 cells were then plated to achieve final 60-70% confluency by the time of IF processing. Cells were washed with 1x PBS 3 times, then fixed in 4% PFA for 10 min at room temperature in the dark. PFA was washed with 1x PBS for another 3 times. Cells were then permeabilized with PBST (1x PBS with 0.25% Triton-X) for 10 min. Cells were then blocked with 5% bovine serum albumin (BSA) in 0.3% Triton-X PBST for 30 min. Cells were then processed for primary antibody staining at 4°C for overnight with a negative control without any primary antibody with indicated antibody dilution shown in the methods section. Antibody staining and washing buffer is 1% BSA in 0.3% PBST. After primary antibody staining, cells were washed for 3 times. Secondary antibody was stained at 1:400 dilution regardless of types of fluorophore conjugated secondary antibody for 1 hr at room temperature along with 1:10,000 dilution of Hoechst 33342. After secondary staining, cells were washed again for 3 times. Last, the coverslips were mounted using Vectashield Vibrance Antifade Mounting Media (H-1700-10). After overnight curing in the

dark at room temperature, the cells were imaged using Zeiss LSM 980 Airyscan 2 microscope and detector equipped with a 63x oil objective with a 1.4 numerical aperture. Post-processing was done with Zen 3.4 (Blue edition).

Proximity ligation assay

Cover glasses (#1.5H Thickness Ø12, Thor Labs) were coated with 0.1mg/ml of poly-D-Lysine (Sigma) for 1 hour at 37°C, washed once with sterile water, dry in the biosafety cabinet for 2 hours, and then complete media was added on to equilibrate for 20 min in the incubator. 25K of HT1080 and 50K of SW480 cells were then plated to achieve final 60-70% confluency by the time of imaging. PLA procedure was conducted via manufacturers protocol using Duolink® In Situ Detection Reagents FarRed (Sigma-Aldrich, cat#-DUO92013) with primary antibody pairs TOM20 and IP3R-I/II/III.

Lattice Light sheet imaging

Same cell conditions were used as live cell confocal imaging. Zeiss Lattice Light Sheet 7 were used and imaged with 20x objective with an NA of 1.0. Cells were treated with fedratinib and then monitored for 16 hr with images getting acquired every 5 min. Initial post-processing was done with Zen 3.4 (Blue edition). Images were deconvolved and then deskewed in the Zen 3.4. (Deskewing transforms the volume into traditional X, Y, Z coordinates.) Then, Arivis Vision 4D (ver. 4.1.0) was used for puncta and cell segmentation. Deconvolved and deskewed datasets were analyzed with Arivis Vision 4D (ver. 4.1.0). For punctas, segmentation was done via the Blob Finder tool. The resulting segments were then filtered by size to remove false positives. For cells, maximum intensity projections of the deconvolved deskewed data were created. Hand segmentations were used to train a machine learning segmentation model. The model was then used to segment each time point in the maximum intensity projection time series. To get the number of cells per time point, the total area of the segments was divided by the average area of a cell. Puncta per cell was then further calculated.

Transmission electron microscopy

SW480 and HT1080 cells treated with vehicle or fedratinib for 24 hr were fixed in 3% glutaraldehyde and 3% paraformaldehyde in 0.1 M cacodylate buffer (CB; pH 7.2) overnight at 4 °C. Cells were then washed with PBS and centrifuged at 2000 rpm for 2 mins. Pre-warmed 2% agarose solution was then carefully added to islet pellets, centrifuged and allowed to cool at 4 °C for 30 min. Samples were then subjected to osmification in 1.5% K4Fe(CN)6 + 2% OsO4 in 0.1 CB for 1 h, dehydrated by serial washes in EtOH (30%, 50%, 70%, 80%, 90%, 95% and 100%) and embedded in Spurr's resin by polymerization at 60 °C for 24 h. Polymerized resins were then sectioned at 90 nm thickness using a Leica EM UC7 ultramicrotome and imaged at 70 kV using a JEOL 1400 TEM equipped with an AMT CMOS imaging system. Cristae classifications were done by blinding all images, and then manually annotated with the four cristae classification: laminar, non-laminar, compartmentalized, and loss-of-cristae. Mitochondrial structures (Aspect Ratio, Perimeter, Circularity) were analyzed and quantified by Fiji/ImageJ. A minimum of 150 mitochondria are analyzed from 25 independent cells.

Correlative light and electron microscopy (CLEM)

SW480 SPLICS reporter cells were induced with doxycycline (100 ng/ml) for 24 hr, and then treated with fedratinib for 24 hr. Cells were high pressure frozen with Leica EM High Pressure Freezer, freeze substituted using 0.1% Uranyl acetate in acetone, and finally infiltrated in Lowicryl HM20, following the protocol published in Ronchi et al., 2021. 300nm sections were cut using a Leica UC7 ultramicrotome and picked up on carbon coated 200 mesh grid**s**. Fluorescence microscopy imaging of the sections was carried out as previously described[65] using a wide-field Olympus IX81, equipped with an Olympus PlanApo 100X 1.4NA oil immersion objective. After that, tilt series of the areas of interest containing fluorescent signal were acquired using a TECNAI F30 (Thermo Fisher Scientific) and tomograms were reconstructed using IMOD.[66] High precision overlays between fluorescence and electron microscopy images were carried out using the plug in ec-CLEM[67] of the software platform Icy,[68] by clicking on corresponding features in the two imaging modalities. These articles were cited for reference[65–68].

Segmentation for CLEM

Automated detection of membranes in the tomogram was performed using the TomoSegMemTV (April 2020 version) software package (PMID: 24625523). The parameters used for membrane enhancement were as follows: scale_space -s 3; dtvoting -s 10 (default); surfaceness -m 0.45 -s 1.0 -p 1.0 (default); dtvoting -w -s 10 (default); surfaceness -S -m 0.3 (default); thresholding -l 0.05; global analysis -3 100 (default). The output volumes were imported into Amira 2022.2 (Thermo Fisher Scientific), and segmented membrane pixels were manually annotated as specific organelle membranes using the 3D magic wand tool and saved as different labels. Further, gaps in the segmentation were filled using the paint tool. The final membrane surfaces were generated using the 'generate surface' module and smoothened using the 'smooth surface' module with the following parameters: iterations 100; lambda 0.2.

High pressure freezing, FIB-SEM, and data processing

Cells were cultured on optically flat sapphire disks (3mm diameter, 50–80um thick, Nanjing Co-Energy Optical Crystal Co., Ltd.). Cell growth media was exchanged 3x for freezing media containing Fluorobrite media (A1896702; ThermoFisher), 25% Dextran (Mr ~40,000, 31389–100G; Sigma), and 0.8pM TetraSpeck microspheres (0.2μm diameter, T7280; Invitrogen). They were then immediately subjected to High Pressure Freezing (HPF Compact 01; Wohlwend GmbH) according to the manufacturer's instructions. Samples were then stored in liquid N_2. Samples were loaded onto a custom CryoSIM microscope as described in the following

citation at the end of the paragraph. Epi-fluorescence montage images were taken of each coverslip to select cells for higher-resolution structured illumination microscopy (SIM). 3D SIM images were acquired (5 phases, 3 angles) over a 7-10um z-depth, and were reconstructed as described in the following citation at the end of the paragraph. Typical reconstruction parameters included 0.007 Wiener Filter, 0.7 gamma apodization, 15-pixel radii of the singularity suppression at the OTF origins. From SIM images, candidate cells for FIB-SEM were selected. Samples were subjected to a freeze-substitution/resin-embedding procedure in 2% OsO_4, 0.1% Uranyl Acetate, and 3% water in acetone under liquid N_2 using a Leica AFS system. Samples were infiltrated and embedded with Eponate 12 resin as described in in the following citation at the end of the paragraph. After coverslips were removed from the resin block (leaving cells embedded), repeated ultramicrotome trimming (Leica EM UC7) and micro X-ray CT imaging (Zeiss Xradia 510) was used in conjunction with cryo-fluorescence image registration to locate the cells of interest in the resin block. Samples were mounted on a copper stud, and sputter coated with 10nm gold and 100nm carbon (PECS 682; Gatan). Samples were loaded onto a custom FIB-SEM, consisting of a Zeiss Gemini 450 Field Emission SEM and a Zeiss Capella FIB column oriented at 90 degrees to the SEM beam.[69]Samples were imaged using 0.9kV landing energy and 0.25nA electron dose, and images were acquired at 200kHz readout rate (5us dwell time), and 4nm pixel size. Samples were milled using a 15nA gallium source at 30kV acceleration voltage. Actual milling time and current per slice was adjusted to maintain average 4nm milling rate, producing isotropic 4nm datasets. Images slices were registered with respect to each other using a python implementation of the SITF algorithm[70] with RANSAC solver and a regularized affine transformation model, available at https://github.com/gleb-shtengel/FIB-SEM. Images were further de-noised using the noise 2 void 2 (N2V2) algorithm, available at https://github.com/juglab/n2v. Overall, similar workflow was performed in these cited publications.[69,71,72]

Segmentation and analysis of FIBSEM

The ER and mitochondria were segmented using deep-learning based segmentation software Empanada (EM Panoptic Any Dimension Annotation).[54] The pretrained MitoNet model was finetuned for instance-based segmentation of mitochondria. A new model was trained for ER segmentation. Semantic and instance-based segmentations were generated for ER and mitochondria, respectively. Instance-based segmentation allowed assignment of unique identifier to each mitochondrion. The mitochondrial segmentations were further improved by manually deleting the falsely segmented objects. The ER segmentations were cleaned by removing unspecific objects less than 2000 pixel2. Following this, the segmentations were further improved by manually deleting larger false positive objects. The segmentations were binned by a factor of 4 for analysis in Fiji. Mitochondrial volumes and ERMCS distances were calculated using the 3D manager plugin. For the quantification of ER-mitochondria contact surface area, single-voxel-thick outer mitochondrial surfaces were generated. Then, the ER objects were expanded by a distance of 64 nm (4 voxels). The overlapping voxels of the expanded ER objects and mitochondria surface were marked as the contact surface. The percentage of mitochondrial contact surface area was calculated by dividing the contact surface area by the total mitochondrial surface area. Training data examples to demonstrate our ER and mitochondria segmentation model can be provided.

Sample preparation for LC-MS/MS metabolomics and lipidomics analysis

Samples for metabolomics and lipidomics LC-MS/MS analyses were prepared by following the automated dual-metabolite/lipid sample preparation workflow described in the Agilent application note 5994-5065EN. Briefly, cells (ca. 1M) were collected, washed with PBS and lysed with 1:1 trifluoroethanol/water at room temperature. Lysates were transferred to microcentrifuge tubes, incubated for 10 minutes, quickly centrifuged at 250 xg for 30 seconds, and dried out by centrifugation under reduced pressure with no heat. Samples were resuspended with 1:1 trifluoroethanol/water, transferred to a 96-well plate, and processed on a Bravo Metabolomics sample preparation platform (Agilent Technologies, Inc.) with two separate VWorks protocols to sequentially and selectively isolate cell metabolites and lipids as described (5994-5065EN).

LC-MS/MS metabolomics and lipidomics analysis

Samples were analyzed on an Agilent 1290 Infinity II Bio LC ultra-high performance liquid chromatography (UPLC) system consisting of a high-pressure binary pump, multicolumn thermostat, and a temperature controlled multisampler. The LC modules were setup with a standard configuration for omics workflows, which allowed easy acquisition method interchange for polar metabolites and lipid analyses. Samples for both targeted metabolomics and lipidomics analysis were analyzed in randomized order on an Agilent 6495C triple quadrupole mass spectrometer equipped with an Agilent Jet Stream Dual ESI ion source. For targeted metabolomics, isolated polar metabolites were analyzed with a HILIC LC-MS/MS method as described in the Agilent application note 5994–5628EN. For targeted lipidomics analysis, samples were analyzed with the reverse phase LC-MS/MS method reported in the Agilent application note 5994-3747EN. After acquisition, both metabolomics and lipidomics datasets were processed with MassHunter Quantitative analysis software and subsequently imported into Mass Profiler Professional (MPP) for chemometrics analysis. Metabolomics and lipidomics data were analyzed using MetaboAnalyst .[55] In particular, statistical analysis [one factor] was selected. Data table with metabolite peak intensities in rows and samples in column was used. Data were filtered based on interquartile range (IQR) set filter out 25%, normalized based on protein quantitation, transformed with Log base 10, scaled by mean-centering and dividing by the standard deviation of each variable. Data were visualized with principal component analysis (PCA) and volcano plots.

Mitochondrial lipidomics

Mitochondria were isolated with the same method detailed prior. Lipid extraction was performed as described by Bielawski[73] with slight modifications. Samples were thawed on ice and then samples were extracted with 1.0 mL of IPA:Water:EtOAc (30:10:60, v:v:v) and internal standard mixture of EquiSPLASH™ LIPIDOMIX® Quantitative Mass Spec Internal Standard (Avanti Polar Lipids, Birmingham, AL). The extract was vortexed and sonicated 2 minutes, followed by centrifugation for 10 minutes at 8000 x g at 4 °C. The organic upper phase was transferred to a new tube. The pellet was re-extracted with an additional 0.5 mL of IPA:Water:EtOAc (30:10:60, v:v:v). The supernatants were combined and placed at -20 °C for 24 h. The supernatants were dried down using a speed vac. The dried sample was reconstituted in 150 μL of the initial condition of the mobile phase. The suspension was vortexed for 5 minutes and then centrifuged for 10 minutes at 17000 x g at 4 °C. The supernatant was transferred to an auto-sampler vial for UHPLC-MS analysis.

Lipid profiling was conducted using a Vanquish UHPLC system with an Orbitrap Fusion Lumos Tribrid™ mass spectrometer using a H-ESI™ ion source (all Thermo Fisher Scientific, Waltham, MA) with a Waters ACQUITY UPLC CSH C18 column (150 mm x 1mm, 1.7 μm particle size, Milford, MA). Solvent A was HPLC grade Water:acetonitrile (40: 60, v:v) with 0.1% formic acid and 10 mM ammonium formate. Solvent B was HPLC grade isopropanol:acetonitrile (95:5, v:v) with 0.1% formic acid and 10 mM ammonium formate. The column was maintained at 65 °C and a flow rate was set at of 110 μL/min. The gradient of the solvent B is 15 % (B) at 0 min, 30 % (B) at 2 min, 2–2.5 min 48% (B), 2.5–11 min 82 % (B), 11–11.01 min 99 % (B), 11.01–12.95 min 99 % (B), 12.95–13 min 15 % (B), and 13–15 min 15 % (B). Data acquisition was carried out in positive and negative charge modes, with the ion source spray voltage configured to 4,000 V and 3,000 V, respectively. The mass spectrometry analysis spanned a scan range of 200 to 1600 m/z for the full scan, and the MS1 resolution was established at 120K at m/z 200. The AcquireX deep scan mode was employed for the MS2 acquisition, which was performed with a stepped collision energy (SCE) of 30%, along with a 5% spread for the positive fragment ion MS/MS scan and with a SCE of 40 % along with a 20 % spread for the negative fragmental scan.

Raw data was converted into mzML format using Proteowizard msconvert software.[56] MS-DIAL software (version v5.4.241004)[57] was used for general lipidomics data analysis including compound identification with LipidBlast[74,75] which is default library in MS-DIAL. The data was normalized by EquiSPLASH spiked-in internal standards.

Targeted CoQ Measurement by LC-MS/MS

Determination of the CoQ content and redox state in mammalian cell culture and isolated mitochondria (with described isolation process) was performed as previously described with modifications. In brief, frozen cell pellets or mitochondria pellets were resuspended in 200 μL of PBS and added to ice cold extraction solution (200 μL acidified methanol [0.1% HCl final], 300 μL hexane, with 0.1 μM CoQ_8 internal standard). Samples were vortexed and centrifuged (5 min, 17000 x g, 4°C) and the top hexane layer was transferred to a new tube. Extraction was repeated twice before the hexane layers were combined and dried under argon gas at room temperature. Extracted dried lipids were resuspended in methanol containing 2 mM ammonium formate and overlaid with argon.

LC-MS analysis was performed using a Thermo Vanquish Horizon UHPLC system coupled to a Thermo Exploris 240 Orbitrap mass spectrometer. For LC separation, a Vanquish binary pump system (Thermo Fisher Scientific) was used with a Waters Acquity CSH C18 column (100 mm × 2.1 mm, 1.7 μm particle size) held at 35 °C under 300 μL/min flow rate. Mobile phase A consisted of 5 mM ammonium acetate in acetonitrile:H_2O (70:30, v/v) with 125 μL/L acetic acid. Mobile phase B consisted of 5 mM ammonium acetate in isopropanol:acetonitrile (90:10, v/v) with the same additive. For each sample run, mobile phase B was initially held at 2% for 2 min and then increased to 30% over 3 min. Mobile phase B was further increased to 50% over 1 min and 85% over 14 min and then raised to 99% over 1 min and held for 4 min. The column was re-equilibrated for 5 min at 2% B before the next injection. Five microliters of the sample were injected by a Vanquish Split Sampler HT autosampler (Thermo Fisher Scientific), while the autosampler temperature was kept at 4 °C. The samples were ionized by a heated ESI source kept at a vaporizer temperature of 350 °C. Sheath gas was set to 50 units, auxiliary gas to 8 units, sweep gas to 1 unit, and the spray voltage was set to 3500 V for positive mode and 2500 V for negative mode. The inlet ion transfer tube temperature was kept at 325 °C with 70% RF lens. For targeted analysis, the MS was operated in parallel reaction monitoring mode with polarity switching acquiring scheduled, targeted scans to oxidized CoQ_{10} H+ adduct (m/z 863.6912), oxidized CoQ_{10} NH+ adduct (m/z 880.7177), reduced $CoQ_{10}H_2$ H+ adduct (m/z 865.7068), reduced $CoQ_{10}H_2$ NH+ adduct (m/z 882.7334), CoQ_8 H+ adduct (m/z 727.566) and CoQ intermediates: DMQ_{10} H+ adduct (m/z 833.6806), and $PPHB_{10}$ H- adduct (m/z 817.6504). MS acquisition parameters include resolution of 15,000, HCD collision energy (30% for positive mode and stepped 20%, 40%, 60% for negative mode), and 3s dynamic exclusion. Automatic gain control targets were set to standard mode. The resulting CoQ intermediate data were processed using TraceFinder 5.1 (Thermo Fisher Scientific). Raw intensity values were normalized to the CoQ_8 internal standard and protein content as determined by BCA.[76]

FACS sorted mitochondrial protein proteomics

All samples were lysed in lysis buffer (8M Urea, 4-(2-Hydroxyethyl)-1-piperazinepropanesulfonic acid (EPPS)) with sonication. Samples were precipitated with SP3 beads and labeled with iodoacetamide, washed and resuspended in 100mM EPPS buffer, pH 8.5 and digested at 37C with trypsin/LysC overnight. The samples were labeled with TMT Pro and quenched with hydroxylamine. All the samples were combined and desalted using a 50 mg Sep-Pak cartridge, followed by drying in a speedvac. Samples were desalted via StageTip and dried with speedvac. Samples were resuspended in 5% formic acid, and 5% acetonitrile for LC-MS/MS analysis.

Mass spectrometry data were collected using a Orbitrap Astral mass spectrometer (Thermo Fisher Scientific, San Jose, CA) coupled with Neo Vanquish liquid chromatograph. Peptides were separated on a 110 cm uPAC C18 column (Thermo Fisher

Scientific). For each analysis, we loaded ~0.5 μg onto the column. Peptides were separated using a 150 min gradient of 5 to 29% acetonitrile in 0.125% formic acid with a flow rate of 300 μL/min.

The scan sequence began with an Orbitrap MS^1 spectrum with the following parameters: resolution 120,000, scan range 350−1350 Th, automatic gain control (AGC) target 200%, maximum injection time 50ms, RF lens setting 50%, and centroid spectrum data type. FAIMS was enabled with compensation voltages (CVs): -35V, -45V, -55V, -60V, and -70V using TopSpeed setting of 1 sec for each CV. We selected the top twenty precursors for MS^2 analysis which consisted of HCD high-energy collision dissociation with the following parameters: Astral data acquisition (TMT off), AGC 200%, maximum injection time 15ms, isolation window 1.2 Th, normalized collision energy (NCE) 36, and centroid spectrum data type. In addition, unassigned and singly charged species were excluded from MS^2 analysis and dynamic exclusion was set to 90 s.

Whole cell proteomics

All samples were labeled with iodoacetamide and resuspended in 100 mM of 4-(2-hydroxyethyl)-1-piperazinepropanesulfonic acid (EPPS) buffer, pH 8.5 and digested at 37C with trypsin/LysC overnight. The samples were labeled with TMT Pro and quenched with hydroxylamine. All the samples were combined and desalted using a 100mg Sep-Pak cartridge, followed by drying in a speedvac. Samples were fractionated with basic pH reversed phase (BPRP) high-performance liquid chromatography (HPLC) as described previously.[77] Samples were desalted via StageTip and dried with a speedvac. Samples were resuspended in 5% formic acid, and 5% acetonitrile for LC-MS/MS analysis. The mass spectrometry proteomics data have been deposited to the ProteomeXchange Consortium via the PRIDE partner repository with the dataset identifier PXD056917.

Liquid chromatography and tandem mass spectrometry

Mass spectrometric data were collected on an Exploris480 mass spectrometer coupled to a Proxeon NanoLC-1200 UHPLC. The 100 μm capillary column was packed with 35 cm of Accucore 150 resin (2.6 μm, 150Å; ThermoFisher Scientific) at a flow rate of 450 nL/min for 90min. The scan sequence began with an MS1 spectrum (Orbitrap analysis, resolution 60,000, 350–1350 th, automatic gain control (AGC) target is set to "standard", maximum injection time set to "auto"). Data were acquired for 150 minutes per analysis. The hrMS2 stage consisted of fragmentation by higher energy collisional dissociation (HCD, normalized collision energy 32%) and analysis using the Orbitrap (AGC 300%, maximum injection time 96 ms, isolation window 0.7 Th, resolution 30,000 with TurboTMT activated). Data were acquired using the FAIMSpro interface the dispersion voltage (DV) set to 5,000V with compensation voltages (CVs) set at -40V, -60V, and -80V. The TopSpeed parameter was set at 1 sec per CV.

Proteomics data analysis

Raw files were searched using the Comet algorithm with a custom database search engine reported previously.[78] Database searching included human (Homo Sapiens) entries from UniProt (http://www.uniprot.org, downloaded 2021) with the reversed sequences, and common contaminants (*i.e.,* keratins, trypsin). Peptides were searched using the following parameters: 50 ppm precursor mass tolerance; up to 2 missed cleavages; variable modifications: oxidation of methionine (+15.9949); static modifications: TMTpro (-+304.2071) on lysine and peptide N terminus, carboxyamidomethylation (+57.0215) on cysteines. The protein-level FDR was determined using the ModScore algorithm where a score of 13 corresponds to 95% confidence in correct localization. TMT reporter ions were used for quantification of peptide abundance. Isotopic impurities were corrected according to the manufacturer's specifications, and signal-to-noise (S/N) was calculated. For Astral MS data, samples were processed by removing peptides with summed S/N lower than 1000 across all channels or isolation specificity lower than 0.7. Spectra with resolution <45,000 were discarded. For samples acquired with Exploris 480, peptides with summed S/N lower than 100 across all channels or isolation specificity lower than 0.7 were excluded. The high confidence peptides were then used to quantify protein abundance by summing up S/N values for all peptides assigned to the same protein, and only proteins in the linear quantification range of the instrument were included in the analysis. The normalization for protein quantification was then performed by adjusting protein loadings of total sum of S/N values to that of every TMT channel.

Chromatin immunoprecipitation (ChIP) Chromatin immunoprecipitation (ChIP) experiments were performed using the Ideal ChIP-seq kit for transcription factors (Diagenode) as per the manufacturer's protocol. 4 million SW480 and HT1080 cells treated with vehicle (DMSO), thapsigargin or fedratinib were used per ChIP reaction with 8ug of the BRD4 antibody (Diagenode, Cat# C15410337). Briefly, cells were crosslinked for 10 minutes in a 1% formaldehyde solution, followed by termination with 1/10th the volume of 1.25M glycine for 5 minutes at room temperature. Following this, the cells were lysed and sonicated (Bioruptor Pico, Diagenode) to obtain desired chromatin fragments of about 200bp. Sheared chromatin was then incubated with the BRD4 antibody overnight at 4 °C. Next day, ChIP-DNA was de-crosslinked and purified using the Diagenode iPure Kit V2, following the manufacturer's protocol. Utilizing the manufacturer's instructions (Illumina), purified DNA was prepared for sequencing. About 1–10ng of ChIP DNA were converted to blunt-ended fragments using T4 DNA polymerase, *Escherichia coli* DNA polymerase I large fragment (Klenow polymerase), and T4 polynucleotide kinase (New England Biolabs (NEB)). Klenow fragment (3′ to 5′ exo minus; NEB) was used to add a single adenine base to fragment ends, followed by ligation of Illumina adaptors (Quick ligase, NEB). PCR enriched the adaptor-ligated DNA fragments using the Illumina Barcode primers and Phusion DNA polymerase (NEB). PCR products were size-selected using 3% NuSieve agarose gels (Lonza) followed by gel extraction using QIAEX II reagents (Qiagen). Quantified libraries quality-checked using the Bioanalyzer 2100 (Agilent) and sequenced on the Illumina HiSeq 2500 Sequencer (125-nucleotide

read length). Reads were first processed using Trimmomatic version 0.39 (settings TruSeq3-PE-2.fa:2:30:10, minlen 50) followed by alignment with bwa ("bwa mem," options -5SP -T0, version 0.7.17-r1198-dirty) to hg38 (GRCh38) reference[58,79]. After alignment the reads were filtered using Markduplicates from Picard and then by quality score of >20 via SAMtools. MACS2 was used to call peaks, filtered using bedtools, and converted to bigwigs with UCSC wigtoBigwig.[59,80] Cistrome overlap analysis was performed in R (v3.6.0) using ChIPpeakAnnoAnno (v3.0.0) and ChipSeeker (v1.29.1).[60,61] Enrichment heatmaps were generated using Deeptools .[62]

RNA Extraction, Reverse Transcription, Real-time PCR and Bromouridine nascent mRNA-Sequencing

RNA was extracted from SW480 and HT1080 cells using the Qiagen RNeasy mini kit according to the manufacturer's instructions. 1 ug of RNA was reverse transcribed using the Lunascript SuperMix (NEB) according to the manufacturer's instructions. Quantitative real-time PCR (qPCR) from cDNA was performed using SYBR Green master mix and beta actin (ACTB) was used as a control. qPCR from BRD4 ChIP-DNA was performed using 1% of input genomic DNA with two sets of primers targeting MYC PVT enhancer locus, and a control primer set targeting an upstream region that does not have BRD4 occupancy. The primer sequences are listed in Table S7. BrU-Seq method is described in these papers.[81,82]

Drug treatment: Small molecule inhibitors used in this studied are listed in the key resources table. Concentration of each compound is listed in figure legend other than fedratinib. Fedratinib was used at 1 μM for all studies unless indicated differently.

Figure Illustrations

Figures were created using Adobe Illustrator and Biorender.com.

QUANTIFICATION AND STATISTICAL ANALYSIS

Each cell line experiment was performed in technical replicates for each condition and repeated at least three times with biological triplicates to ensure reproducibility. Figures show a representative biological replicate unless otherwise indicated. Blinding was performed whenever appropriate. Sample description and identification was unavailable to the core personnel during data collection and analysis. Statistical details of all experiments can be found in the figure legends. The sample numbers are mentioned in each figure legend and denote biological replicates. Results are expressed as the mean plus or minus the standard error of the mean for all figures unless otherwise noted. Significance between 2 groups was tested using a 2 tailed unpaired t test. Significance among multiple groups was tested using a one-way ANOVA with Tukey correction for multiple comparisons. GraphPad Prism 10.6.1 was used for the statistical analysis. Statistical significance is described in the figure legends as: * $p < 0.05$, ** $p < 0.01$, *** $p < 0.005$, **** $p < 0.001$.